Inclusive quarkonium production in pp collisions at √s = 5.02 TeV

(ALICE Collaboration) Acharya, S.; ...; Erhardt, Filip; ...; Gotovac, Sven; ...; Jerčić, Marko; ...; Karatović, David; ...; ...

Regular Article - Experimental Physics

Inclusive quarkonium production in pp collisions at $\sqrt{s}$ = 5.02 TeV

ALICE Collaboration*

CERN, 1211 Geneva 23, Switzerland

Abstract This article reports on the inclusive production cross section of several quarkonium states, J/ψ, ψ(2S), Υ(1S), Υ(2S), and Υ(3S), measured with the ALICE detector at the LHC, in pp collisions at $\sqrt{s}$ = 5.02 TeV. The analysis is performed in the dimuon decay channel at forward rapidity (2.5 < y < 4). The integrated cross sections and transverse-momentum (p_T) and rapidity (y) differential cross sections for J/ψ, ψ(2S), Υ(1S), and the ψ(2S)-to-J/ψ cross section ratios are presented. The integrated cross sections, assuming unpolarized quarkonia, are: $\sigma_{J/\psi}$ (p_T < 20 GeV/c) = 5.88 ± 0.03 ± 0.34 μb, $\sigma_{\psi(2S)}$ (p_T < 12 GeV/c) = 0.87 ± 0.06 ± 0.10 μb, $\sigma_{\Upsilon(1S)}$ (p_T < 15 GeV/c) = 45.5 ± 3.9 ± 3.5 nb, $\sigma_{\Upsilon(2S)}$ (p_T < 15 GeV/c) = 22.4 ± 3.2 ± 2.7 nb, and $\sigma_{\Upsilon(3S)}$ (p_T < 15 GeV/c) = 4.9 ± 2.2 ± 1.0 nb, where the first (second) uncertainty is the statistical (systematic) one. For the first time, the cross sections of the three Υ states, as well as the ψ(2S) one as a function of p_T and y, are measured at $\sqrt{s}$ = 5.02 TeV at forward rapidity. These measurements also significantly extend the J/ψ p_T reach and supersede previously published results. A comparison with ALICE measurements in pp collisions at $\sqrt{s}$ = 2.76, 7, 8, and 13 TeV is presented and the energy dependence of quarkonium production cross sections is discussed. Finally, the results are compared with the predictions from several production models.

1 Introduction

Quarkonium production in high-energy hadronic collisions is an important tool to study the perturbative and non-perturbative aspects of quantum chromodynamics (QCD) calculations [1,2]. Quarkonia are bound states of either a charm and anti-charm (charmonia) or a bottom and anti-bottom quark pair (bottomonia). In hadronic collisions, the scattering process leading to the production of the heavy-quark pair involves momentum transfers at least as large as twice the mass of the considered heavy quark, hence it can

be described with perturbative QCD calculations. In contrast, the binding of the heavy-quark pair is a non-perturbative process as it involves long distances and soft momentum scales. Describing quarkonium production measurements in proton–proton (pp) collisions at various colliding energies represents a stringent test for models and, in particular, for the investigation of the non-perturbative aspects that are treated differently in the various approaches. These measurements also provide a crucial reference for the investigation of the properties of the quark–gluon plasma formed in nucleus–nucleus collisions and of the cold nuclear matter effects present in proton–nucleus collisions [2,3].

Quarkonium production can be described by various approaches that essentially differ in the treatment of the hadronization part. The Color Evaporation Model (CEM) [4,5] considers that the quantum state of every heavy-quark pair produced with a mass above its production threshold and below twice the open heavy flavor (D or B meson) threshold production evolves into a quarkonium. In this model, the probability to obtain a given quarkonium state from the heavy-quark pair is parametrized by a constant phenomenological factor. The Color Singlet Model (CSM) [6] assumes no evolution of the quantum state of the pair from its production to its hadronization. Only color-singlet heavy-quark pairs are thus considered to form quarkonium states. Finally, in the framework of Non-Relativistic QCD (NRQCD) [7], both color-singlet and color-octet heavy-quark pairs can evolve towards a bound state. Long Distance Matrix Elements are introduced in order to parametrize the binding probability of the various quantum states of the heavy-quark pairs. They can be constrained from existing measurements and do not depend on the specific production process under study (pp, electron–proton, etc.).

This article presents measurements of the inclusive production cross section of charmonium (J/ψ and ψ(2S)) and bottomonium (Υ(1S), Υ(2S), and Υ(3S)) states in pp collisions at a center-of-mass energy $\sqrt{s}$ = 5.02 TeV with the ALICE detector. The analysis is performed in the dimuon decay channel at forward rapidity (2.5 < y < 4). In this

*e-mail: alice-publications@cern.ch

rapidity interval, the total, transverse momentum (p_T) and rapidity (y) differential cross sections for J/ψ as well as the total cross section for ψ(2S), were published by the ALICE collaboration based on an earlier data sample [8,9], corresponding to a factor 12 smaller integrated luminosity. These measurements with improved statistical precision supersede the ones from earlier publication. The p_T and y differential measurements for the ψ(2S) and Υ(1S) as well as the total cross sections for all the measured Υ states are presented here for the first time at $\sqrt{s}$ = 5.02 TeV and at forward rapidity. The p_T coverage of the J/ψ measurement is extended up to 20 GeV/c.

The inclusive differential cross sections are obtained as a function of p_T for p_T < 20 GeV/c and as a function of y for p_T < 12 GeV/c for J/ψ, for p_T < 12 GeV/c for ψ(2S), and for p_T < 15 GeV/c for Υ(1S). Only the p_T-integrated cross sections are measured for Υ(2S) and Υ(3S) due to statistical limitations. The inclusive ψ(2S)-to-J/ψ ratio is also presented as a function of p_T and y. The comparison of the J/ψ cross section with recent results from LHCb [10] is discussed. The results are compared with previous ALICE measurements performed at $\sqrt{s}$ = 2.76, 7, 8, and 13 TeV [9,11–13]. Earlier comparisons with LHCb quarkonium results at $\sqrt{s}$ = 7, 8, and 13 TeV [14–17] were performed in [9,12,13]. Finally, the results are compared with theoretical calculations based on NRQCD and CEM.

The measurements reported here are inclusive and correspond to a superposition of the direct production of quarkonium and of the contribution from the decay of higher-mass excited states (predominantly ψ(2S) and χ_c for J/ψ, Υ(2S), χ_b, and Υ(3S) for Υ(1S), Υ(3S) and χ_b for Υ(2S), and χ_b for Υ(3S)). For J/ψ and ψ(2S) a non-prompt contribution from beauty hadron decays is also present.

The article is organized as follows: the ALICE detectors used in the analysis and the data sample are briefly described in Sect. 2, the analysis procedure is presented in Sect. 3, and in Sect. 4 the results are discussed and compared with theoretical calculations and measurements at other center-of-mass energies from ALICE.

2 Apparatus and data samples

A detailed description of the ALICE setup and its performance are discussed in Refs. [18,19]. In this section, the subsystems relevant for this analysis are presented.

Muons from quarkonium decays are detected in the muon spectrometer within the pseudorapidity range[1] $-4 <$

$\eta < -2.5$ [20]. The muon spectrometer consists of a front absorber located along the beam direction (z) between -0.9 and -5 m from the interaction point (IP), five tracking stations (MCH), located between -5.2 and -14.4 m from the IP, an iron wall at -14.5 m, and two triggering stations (MTR), placed at -16.1 and -17.1 m from the IP. Each station is made of two layers of active detection material, with cathode pad and resistive plate techniques employed for the muon detection in the tracking and triggering devices, respectively. A dipole magnet with a 3 T×m field integral deflects the particles in the vertical direction for the measurement of the muon momentum. The hadronic particle flux originating from the collision vertex is strongly suppressed thanks to the front absorber with a thickness of 10 interaction lengths. Throughout the spectrometer length, a conical absorber at small angle around the z axis reduces the background from secondary particles originating from the interaction of large angle primary particles with the beam pipe. The 1.2 m thick iron wall positioned in front of the triggering stations stops the punch-through hadrons escaping the front absorber, as well as low-momentum muons from pion and kaon decays. In addition, a rear absorber downstream of the trigger stations ensures protection against the background generated by beam–gas interactions.

Two layers of silicon pixel detectors (SPD) with a cylindrical geometry, covering $|\eta| < 2.0$ and $|\eta| < 1.4$, respectively, are used for the determination of the collision vertex. They are the two innermost layers of the Inner Tracking System (ITS) [21] and surround the beam pipe at average radii of 3.9 and 7.6 cm. The T0 quartz Cherenkov counters [22] are made of two arrays positioned on each side of the IP at -70 cm and 360 cm. They cover the pseudorapidity ranges $-3.3 < \eta < -3.0$ and $4.6 < \eta < 4.9$, respectively. The T0 is used for luminosity determination and background rejection. Similarly, the V0 scintillator arrays [23] are located on both sides of the IP at -90 and 340 cm and cover the pseudorapidity ranges $-3.7 < \eta < -1.7$ and $2.8 < \eta < 5.1$, respectively. These are used for triggering, luminosity determination and to reject beam–gas events using offline timing selections together with the T0 detectors.

A minimum bias trigger is issued by the V0 detector [23] when a logical AND of signals from the two V0 arrays on each side of the IP is produced. Single muon, same-sign dimuon, and opposite-sign dimuon triggers are defined by an online estimate of the p_T of the muon tracks using a programmable trigger logic circuit. A predefined p_T threshold of 0.5 GeV/c is set in order to remove the low-p_T muons, mainly coming from π and K decays. The muon trigger efficiency reaches 50% at this threshold value and saturates for p_T > 1.5 GeV/c. Events containing an opposite-sign dimuon trigger in coincidence with the minimum bias trigger are selected for the quarkonium analysis.

---

[1] In the ALICE coordinate system, detectors located on the muon spectrometer side are defined as being at negative z (and negative pseudorapidity). However, due to the symmetry of pp collisions, the results are presented at positive rapidity.

The data sample of pp collisions at $\sqrt{s} = 5.02$ TeV used for the measurements reported in this article was collected in 2017 with the opposite-sign dimuon trigger, and corresponds to an integrated luminosity $L_{int} = 1229.9 \pm 0.4$ (stat.) ± 22.1 (syst.) nb^{-1} [24]. The luminosity determination is based on dedicated van der Meer scans [25], where the cross sections seen by two different minimum bias triggers based on the V0 and T0 signals are derived [24]. The number of T0-and dimuon-trigger counts measured with scalers on a run-by-run basis without any data acquisition veto is used along with the T0-trigger cross section to calculate the integrated luminosity of the analyzed data sample. Another method, using reconstructed minimum bias events triggered with the V0 detector only, is used as a cross-check of the first method. In this method, the luminosity is computed as the ratio of the number of equivalent minimum bias events over the V0-trigger cross section. The number of equivalent minimum bias events is evaluated as the product of the total number of dimuon-triggered events with the inverse of the probability of having dimuon-triggered events in a minimum bias triggered data sample recorded with only the V0 [26]. The two methods give compatible values and the one based on T0 is used, as it gives a smaller total uncertainty (see Sect. 3.4).

3 Analysis procedure

3.1 Track selection

The number of detected quarkonia is estimated by pairing muons of opposite charges and by fitting their invariant mass ($m_{\mu^+\mu^-}$) distribution. Reconstructed tracks must meet several selection criteria. The pseudorapidity of each muon candidate must be within the geometrical acceptance of the muon spectrometer ($-4 < \eta < -2.5$). Muons are identified and selected by applying a matching condition between the tracking system and the trigger stations. A selection on the transverse position R_{abs} of the muon at the end of the front absorber ($17.6 < R_{abs} < 89.5$ cm) rejects tracks crossing the thickest sections of the absorber. Finally, the contamination from tracks produced by background events, like beam–gas collisions, is reduced by applying a selection on the product of the track momentum and the transverse distance to the primary vertex [27]. Opposite-sign (OS) muon pairs are then formed in the range $2.5 < y < 4$. The considered p_T interval varies according to the studied resonance given the available data sample: $p_T < 20$ GeV/c for J/ψ; $p_T < 12$ GeV/c for ψ(2S); y-differential and (p_T,y)-differential J/ψ studies; and $p_T < 15$ GeV/c for Υ(nS).

3.2 Signal extraction

A fit to the OS dimuon invariant mass distribution is performed separately for the charmonium and bottomonium

mass regions, in each p_T and y interval considered. In both cases, a maximum log-likelihood fitting method is used. In order to evaluate the systematic uncertainties on the charmonium and bottomonium signal extraction, several fitting functions and ranges are considered, and the parameters that are fixed during the fitting procedure are varied, as described below.

In the charmonium mass region ($2 < m_{\mu^+\mu^-} < 5$ GeV/c^2), the fit is performed using the same functional form to describe the J/ψ and ψ(2S) signals, on top of an ad-hoc function to describe the background. The signal shapes considered are either two extended Crystal Ball functions or two pseudo-Gaussian functions [28]. For both functional forms, the J/ψ mass pole and width are left free during the fit procedure, while the ψ(2S) mass is bound to the J/ψ one by fixing the mass difference between the two states according to the PDG values [29]. The width of the ψ(2S) signal is also bound to the J/ψ one by means of a scale factor on their ratio. It was obtained via a fit to a large data sample from pp collisions at $\sqrt{s} = 13$ TeV [9] which gives 1.01 ± 0.05. A variation of $+5\%$ of the ψ(2S)-to-J/ψ width ratio central value, corresponding to the difference observed between data and Monte Carlo (MC) simulation at $\sqrt{s} = 13$ TeV,[2] induces a variation of the J/ψ yield at the per mille level and is therefore neglected, while the impact of this variation on the ψ(2S) yield enters the systematic uncertainty. The parameters describing the left and right signal tails are the same for both resonances and are fixed to the values extracted from either MC simulations at $\sqrt{s} = 5.02$ TeV using the GEANT3 [30] or the GEANT4 [31] transport codes (see Sect. 3.3), or from fits to the 13 TeV data sample. While the tail parameters can be extracted in p_T and y intervals in the MC for both signal shapes, the 13 TeV data sample is only used to constrain the tail parameters of the extended Crystal Ball, when performing a fit to the invariant mass spectrum integrated over p_T and y. Therefore, when using tail parameters from data, the same set is applied to all the p_T and y intervals. Various functions successfully model the background in the invariant mass range $2 < m_{\mu^+\mu^-} < 5$ GeV/c^2. To extract the J/ψ signal, either a pseudo Gaussian with a width increasing linearly with the invariant mass or the ratio of a first order to second order polynomial is used as a background shape. For the ψ(2S) signal extraction, either a pseudo Gaussian with a width increasing linearly with the invariant mass or the combination of a fourth order polynomial with an exponential function is used to describe the background. In addition to the variation of the background shapes, two different fitting ranges are also used for the evaluation of the signal extraction systematic uncertainties. For each p_T and y range, several fits

---

[2] It is assumed that the ψ(2S)-to-J/ψ width ratio and signal tail parameters do not depend on the collision energy and are the same at $\sqrt{s} = 5.02$ TeV and $\sqrt{s} = 13$ TeV.
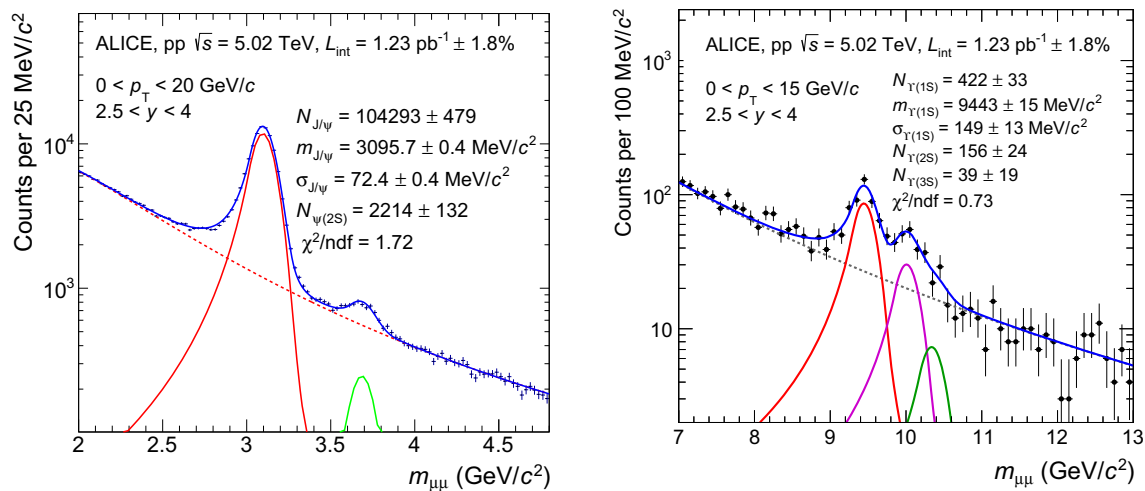
Fig. 1 Examples of fit to the OS dimuon invariant mass distribution in the mass region $2 < m_{\mu^+\mu^-} < 5$ GeV/c^2 for $p_T < 20$ GeV/c (left), and $7 < m_{\mu^+\mu^-} < 13$ GeV/c^2 for $p_T < 15$ GeV/c (right). The J/ψ, ψ(2S) and Υ(nS) signals are modelled with extended Crystal Ball functions, while the background is described by a pseudo Gaussian with a width increasing linearly with the invariant mass. The fit is performed on the full data sample. The widths of the ψ(2S), Υ(2S) and Υ(3S), for these examples, are fixed to 73 MeV/c, 156 MeV/c and 161 MeV/c, respectively

are performed with different combinations of signal shapes, background shapes, fitting ranges, signal tail parameters, and signal width ratios between the two resonances for the ψ(2S) case. For the charmonium states, the raw yields are computed as the weighted average of the results of all the fits. The statistical uncertainty is the weighted average of the statistical uncertainties of the fits, while the systematic uncertainty is taken as the RMS of the distribution of the results. Given that the choice of the signal tails is the main source of systematic uncertainty, this weight is applied to counterbalance the higher number of fits performed with MC tails with respect to fits with data-driven tails. The raw J/ψ yield is $N_{J/\psi} = 101285 \pm 452$ (stat.) ± 3012 (syst.) for $p_T < 20$ GeV/c, and the ψ(2S) raw yield is $N_{\psi(2S)} = 2086 \pm 133$ (stat.) ± 150 (syst.) for $p_T < 12$ GeV/c. Figure 1 left shows an example of a fit of the OS dimuon invariant mass distribution in the mass region $2 < m_{\mu^+\mu^-} < 5$ GeV/c^2, separately showing the contributions of the two charmonium resonances and the background. In each p_T and y interval, the ψ(2S)-to-J/ψ yield ratio is evaluated as the weighted average of the ψ(2S)-to-J/ψ yield ratio values obtained from each individual fits (with a given signal shape, background shape, signal tail choice, fitting range and ψ(2S) width) in order to properly account for correlations in the J/ψ and ψ(2S) signal extraction. The statistical and systematic uncertainties on the ratio are then evaluated in the same way as for the J/ψ and ψ(2S) raw yields.

In the bottomonium mass region ($7 < m_{\mu^+\mu^-} < 13$ GeV/c^2), the Υ(nS) shapes are parametrized only with extended Crystal Ball functions, since it was checked that the systematic uncertainty related to the choice of the sig-

nal shape is negligible compared to other sources. The Υ(1S) mass and width are left free in the fit, while the Υ(2S) and Υ(3S) masses are bound to the Υ(1S) one by fixing the mass difference between the states according to the PDG values [29]. The width of the Υ(2S) and Υ(3S) signals are also bound to the Υ(1S) one by factors, $\sigma_{\Upsilon(nS)}^{MC}/\sigma_{\Upsilon(1S)}^{MC}$, obtained from MC simulations. Two alternative width scalings, namely $\sigma_{\Upsilon(nS)} = \sigma_{\Upsilon(1S)}$ and $\sigma_{\Upsilon(nS)} = \sigma_{\Upsilon(1S)} \times (2 \times \sigma_{\Upsilon(nS)}^{MC}/\sigma_{\Upsilon(1S)}^{MC} - 1)$, are also considered. The Υ(nS) signal tail parameters must also be fixed while fitting. By default, they are fixed to the values extracted in each given p_T and y range from MC simulations performed with the GEANT3 transport code. The same shapes are used for the three Υ resonances. The systematic uncertainty related to the choice of the tail parameters is evaluated for each resonance on the p_T and y integrated mass distribution by using several sets of tail parameters that were generated from the fit of the 13 TeV data sample taking into account the correlation among the parameters via the covariance matrix. This uncertainty is then considered to be the same for all Υ(1S) p_T and y differential intervals. The background shape is described by three empirical functions: an exponential function, a sum of two exponential functions, and a power law function. Additionally, two fit ranges are used. The Υ(nS) raw yields and statistical uncertainties are then computed as the average of all the fit results and statistical uncertainties, respectively. The systematic uncertainty is the RMS of the fit results summed in quadrature with the uncertainty from the choice of signal tails. The main sources of systematic uncertainty come from the choice of the background description and from the choice of the tail parame-

ters. The $\Upsilon(nS)$ raw yields are $N_{\Upsilon(1S)} = 401 \pm 34$ (stat.) ± 26 (syst.), $N_{\Upsilon(2S)} = 153 \pm 22$ (stat.) ± 12 (syst.), and $N_{\Upsilon(3S)} = 38 \pm 17$ (stat.) ± 7 (syst.), for $p_T < 15$ GeV/c. The significance of the $\Upsilon(3S)$ signal remains rather limited and amounts to 2.4. Figure 1 right shows an example of fit to the OS dimuon invariant mass distribution in the mass region $7 < m_{\mu^+\mu^-} < 13$ GeV/c^2 for $p_T < 15$ GeV/c, showing the contribution of the three Υ resonances. Similarly to the charmonium case, the $\Upsilon(2S)$-to-$\Upsilon(1S)$ and $\Upsilon(3S)$-to-$\Upsilon(1S)$ raw yield ratios are extracted on a fit-by-fit basis, in order to account for correlations in the signal extraction.

3.3 Acceptance and efficiency corrections

The detector acceptance and reconstruction efficiency ($A \times \varepsilon$) corrections are applied to the quarkonium raw yields to obtain the corrected yields for the individual resonances. The ($A \times \varepsilon$) values are estimated via MC simulations by computing the ratio between the number of quarkonia reconstructed in the muon spectrometer and the number of generated quarkonia in given p_T and y intervals. Monte Carlo simulations are performed reproducing on a run-by-run basis the detector conditions during the data taking.

In the first stage of the simulation procedure, a parametric generator based on phenomenological p_T and y distributions of quarkonia extracted from RHIC, Tevatron, and LHC data [32] is employed, assuming unpolarized resonance production as suggested by the ALICE [33,34] and LHCb [35–37] measurements on polarization parameters for quarkonia that are found small or compatible with zero. The quarkonium decay to $\mu^+\mu^-$ is implemented using EVTGEN [38] and PHOTOS [39] to account for the radiative decay of the quarkonium states. The decay muons are tracked through a GEANT3 [30] model of the apparatus that includes a realistic description of the detectors and their performance during data taking. An independent test of the detector simulation has also been performed using the GEANT4 [31] framework. It provides ($A \times \varepsilon$) results compatible with the GEANT3 simulation within a maximum deviation of 2%.

The J/ψ, $\psi(2S)$, and $\Upsilon(1S)$ raw yields are divided by the ($A \times \varepsilon$) correction factors to obtain a first estimate of the p_T and y distributions. An iterative procedure is performed to tune the quarkonium input p_T and y MC distributions on the measured data distributions until no significant variation of the input shapes is observed. Because of statistical limitations, the iterative procedure cannot be applied to the $\Upsilon(2S)$ and $\Upsilon(3S)$ as p_T and y-differential measurements cannot be performed. Since no significant variation of the y input shape between the $\Upsilon(nS)$ states is expected [40] and the $\Upsilon(nS)$ ($A \times \varepsilon$) does not strongly depend on the p_T spectrum of the MC input, the $\Upsilon(1S)$ p_T and y shapes are applied for the $\Upsilon(2S)$ and $\Upsilon(3S)$.

3.4 Systematic uncertainties

The main systematic uncertainties on the quarkonium production cross section (see Eq. 1) come from the following sources: (1) the quarkonium signal extraction, (2) the branching ratio, (3) the determination of the luminosity, and (4) the acceptance and efficiency corrections. The uncertainties on the latter can be broken down into the following contributions: (i) the choice of parametrization for the signal input p_T and y distributions, (ii) the tracking efficiency in the muon tracking chambers, (iii) the muon trigger efficiency, and (iv) the matching efficiency between the tracks reconstructed in the muon tracker and the track segments measured in the muon trigger systems.

The evaluation of the systematic uncertainty on quarkonium signal extraction is detailed in Sect. 3.2. It amounts to 3%, 7.2%, 6.5%, 7.8%, and 19% for the integrated J/ψ, $\psi(2S)$, $\Upsilon(1S)$, $\Upsilon(2S)$, and $\Upsilon(3S)$ signals, respectively. This uncertainty is uncorrelated as a function of p_T and y, for a given quarkonium state. It is, however, partially correlated between J/ψ and $\psi(2S)$, and among the three $\Upsilon(nS)$ resonances.

The systematic uncertainty on the branching ratio is taken as the current estimate for this quantity according to the PDG [29] and is reported in Tables 1, 2, and 3 for all the states. This uncertainty is fully correlated versus p_T and y for a given resonance.

Regardless of the method used to determine the luminosity, its associated systematic uncertainty has two origins: the uncertainty on the normalization factor between the number of triggered events and the equivalent number of minimum bias events, and the uncertainty on the cross section of the minimum bias trigger evaluated using the van der Meer scan technique [24]. The first source of uncertainty is evaluated by using minimum bias triggers issued either by the V0 or the T0 detectors. The two methods are in agreement within 0.5%. This systematic uncertainty is therefore consistently neglected for all resonances and the method which uses the T0 detector is used as the main one since it gives the result with the smallest statistical uncertainty. The second source of uncertainty is the dominant one and arises from the uncertainty on the T0-trigger cross section. It amounts to 1.8%. This uncertainty is fully correlated as a function of p_T and y for a given state and also fully correlated among all the quarkonium states.

The systematic uncertainty on ($A \times \varepsilon$) related to the parametrization of the signal input p_T and y distributions has two components. The first one arises from the fact that the corrected yield used to tune the MC input shape in the iterative procedure is obtained from a data sample with an associated statistical uncertainty. This has a negligible impact on the J/ψ and $\psi(2S)$ results, since their reconstructed signals profit from a large sample. For the $\Upsilon(1S)$ state, this

Table 1 Summary of the systematic uncertainties on the J/ψ cross section, integrated over p_T, p_T-differential, y-differential, and double differential in p_T and y. Values marked with an asterisk correspond to uncertainties correlated over p_T and/or y

Source	Integrated (%)	p_T-diff (%)	y-diff (%)	p_T-diff and y-diff (%)
Branching ratio	0.6	0.6*	0.6*	0.6*
Luminosity	1.8	1.8*	1.8*	1.8*
Signal extraction	3	1.9–4.4	2.1–4.4	0.8–4.4
MC input	3.2	0.3–2.2	1.4–4.9	0.1–3.3
MCH efficiency	2	2	2	2
MTR efficiency	2	1.0–2.2	1.0–2.6	1.0–3.1
Matching efficiency	1	1	1	1

Table 2 Summary of the systematic uncertainties on the ψ(2S) cross section, integrated over p_T and y, as well as p_T-differential and y-differential. Values marked with an asterisk correspond to uncertainties correlated over p_T and/or y

Source	Integrated (%)	p_T-diff (%)	y-diff (%)
Branching ratio	7.5	7.5*	7.5*
Luminosity	1.8	1.8*	1.8*
Signal extraction	7.2	5.8–15.4	5.8–13.9
MC input	3.3	1.4–2.4	1.4–5.0
MCH efficiency	2	2	2
MTR efficiency	2	1.4–2.2	1.0–2.6
Matching efficiency	1	1	1

Table 3 Summary of the systematic uncertainties on the Υ(nS) cross section, integrated over p_T and y, as well as p_T-differential and y-differential for the Υ(1S). Values marked with an asterisk correspond to uncertainties correlated over p_T and/or y

	Υ(1S)			Υ(2S)	Υ(3S)
Source	Integrated (%)	p_T-diff (%)	y-diff (%)	Integrated	Integrated
Branching ratio	2.0	2.0*	2.0*	8.8	9.6
Luminosity	1.8	1.8*	1.8*	1.8	1.8
Signal extraction	6.5	6.1–7.0	6.2–7.6	7.8	19
MC input	1.7	1.5–1.7	2.2–3.5	1.7	1.7
MCH efficiency	2	2	2	2	2
MTR efficiency	1.2	1.1–1.5	1.0–1.2	1.2	1.2
Matching efficiency	1	1	1	1	1

uncertainty is not negligible and is evaluated by performing 50 fits to the p_T and y differential corrected yields after having randomly moved each data point according to a Gaussian smearing within the statistical uncertainty of the data point. The RMS of the resulting distribution of the obtained $(A \times \varepsilon)$ values is assigned as the uncertainty. It varies between 1.3% and 3.5%. The second component arises from the fact that the correlations in p_T and y of the quarkonium input shape are not accounted for in the simulation. It is evaluated by performing several fits to the y-differential corrected yields in different p_T intervals, and to the p_T-differential corrected yields in different y intervals. To be conservative, all the possible p_T and y input shape combinations are then con-

sidered, the $(A \times \varepsilon)$ values are evaluated and the RMS of the results gives the associated uncertainty, ranging between 0.3% and 4.9%. Such a study can only be performed for the J/ψ since it requires a large data sample to perform double-differential measurements. For the ψ(2S), the uncertainty from the p_T and y double-differential shape variation is assumed to be the same as for the J/ψ. Moreover, additional p_T and y shapes are considered in the systematic uncertainty evaluation. They are obtained by using the measured J/ψ p_T and y-dependent cross sections times the ψ(2S)-to-J/ψ cross section ratios. This additional contribution is summed quadratically to the J/ψ one and is below 1.5% in all p_T and y intervals. The resulting total MC input shape

systematic uncertainty on the $\psi(2S)$ ranges between 1.4% and 5.0%. Given the absence of p_T and y double-differential Υ measurements at $\sqrt{s} = 5.02$ TeV, an estimation of the variation of the $\Upsilon(1S)$ input shape is performed by fitting the $\Upsilon(1S)$ cross sections measured with high statistical precision by LHCb in pp collisions at $\sqrt{s} = 13$ TeV [41], as a function of y in four p_T bins and as a function of p_T in five y bins. The combination of these 20 input p_T and y distributions is used to assess the systematic uncertainty on the $\Upsilon(1S)$ $(A \times \varepsilon)$ quantity. Its value ranges between 0.5% and 1%. For the $\Upsilon(2S)$ and $\Upsilon(3S)$, the same MC input systematic uncertainty as the $\Upsilon(1S)$ is assumed for the integrated cross section. The two aforementioned sources contributing to the $(A \times \varepsilon)$ uncertainty are uncorrelated and are therefore summed in quadrature, when relevant. The total systematic uncertainty on the $(A \times \varepsilon)$ related to the parametrization of the signal input p_T and y distributions is considered uncorrelated as a function of p_T and y for a given quarkonium state. In addition, it was checked for the J/ψ that using as MC input shapes the ones obtained from the PYTHIA8 generator [42] instead of the parametrization from Ref. [32] was leading to similar results within the uncertainties discussed above.

The systematic uncertainty on the tracking efficiency in the muon chambers is obtained by comparing data with MC simulation. The single-muon tracking efficiency can be derived, in both data and MC, from the chamber efficiency, which can be evaluated using the redundancy of the tracking information in each station, since a subset of the detector is sufficient for a track to be reconstructed [19]. The differences between the data and MC tracking efficiencies are taken as systematic uncertainty. A 1% uncertainty is found at the single muon level, hence a 2% uncertainty applies at the dimuon level for all the resonances. This uncertainty is assumed uncorrelated versus p_T and y.

The systematic uncertainty on the trigger efficiency has two origins: the differences in shape of the p_T-dependence of the trigger response function between data and MC in the region close to the trigger threshold, and the intrinsic efficiencies of the muon trigger chambers. The first uncertainty is estimated by comparing the p_T dependence, at the single-muon level, of the trigger response function between data and MC. This difference is then propagated at the dimuon level in the MC to evaluate the effect on the quarkonium $(A \times \varepsilon)$ determination. The obtained uncertainty varies, as a function of p_T and y, between 0.3% and 2.4% for the J/ψ and $\psi(2S)$, and between 0.3% and 1.1% for the $\Upsilon(nS)$. The second uncertainty is estimated by comparing the $(A \times \varepsilon)$ obtained in the MC, with a second simulation in which the uncertainties on the trigger chamber efficiencies, as measured from data after varying the track selection criteria, are applied at the detector level, taking into account its segmentation, to blur the trigger response. This uncertainty is 1% for all the

quarkonium states. The uncertainty on the trigger efficiency is uncorrelated as a function of p_T and y.

The systematic uncertainty associated to the matching efficiency between the tracks reconstructed in the tracking chambers and those reconstructed in the trigger chambers is evaluated from the comparison of the efficiency variation in data and simulation by varying the value of the χ^2 selection applied on the matching condition. It leads to a systematic uncertainty of 1% common to all the quarkonium resonances, and uncorrelated versus p_T and y.

Tables 1, 2, and 3 summarize the systematic uncertainties on the evaluation of the J/ψ, $\psi(2S)$, and $\Upsilon(nS)$ cross section, respectively. Values marked with an asterisk correspond to uncertainties correlated over p_T and/or y. The total systematic uncertainty for a given quarkonium state is the quadratic sum of all the sources listed in the corresponding table.

The systematic uncertainty on the $\psi(2S)$-to-J/ψ, $\Upsilon(2S)$-to-$\Upsilon(1S)$, and $\Upsilon(3S)$-to-$\Upsilon(1S)$ cross section ratios includes the uncertainty on the signal extraction, MC input, and branching ratio of the resonances. The systematic uncertainties from MCH and MTR efficiencies, and matching efficiency are similar for the ground and excited states and cancel out in the ratio, as do the luminosity uncertainty. The total systematic uncertainty on the integrated $\psi(2S)$-to-J/ψ ratio is 10%, while this systematic uncertainty varies between 9% and 16% as a function of p_T and between 8.9% and 15% as a function of y. The total systematic uncertainty on the integrated $\Upsilon(2S)$-to-$\Upsilon(1S)$ [$\Upsilon(3S)$-to-$\Upsilon(1S)$] ratio is 12% [20%] respectively.

4 Results and discussion

The p_T- and y-differential cross section for inclusive quarkonium production is given by

$$\frac{d^2\sigma}{dp_T dy} = \frac{N(\Delta y, \Delta p_T)}{L_{int} \times BR \times (A \times \varepsilon)(\Delta y, \Delta p_T) \times \Delta p_T \times \Delta y}, \quad (1)$$

where $N(\Delta y, \Delta p_T)$ is the raw quarkonium yield measured in a given p_T and y interval of width Δp_T and Δy, respectively. The dimuon branching ratios BR are $(5.96 \pm 0.03)\%$ for J/ψ, $(0.80 \pm 0.06)\%$ for $\psi(2S)$, $(2.48 \pm 0.05)\%$ for $\Upsilon(1S)$, $(1.93 \pm 0.17)\%$ for $\Upsilon(2S)$, and $(2.18 \pm 0.21)\%$ for $\Upsilon(3S)$ [29].

In this section, the results are given with two uncertainties, the first and second being the statistical and systematic ones, respectively. In the figures, the data points are represented with vertical error bars as statistical uncertainties and with boxes as systematic uncertainties. The correlated systematic uncertainties are quoted as text in the legends.
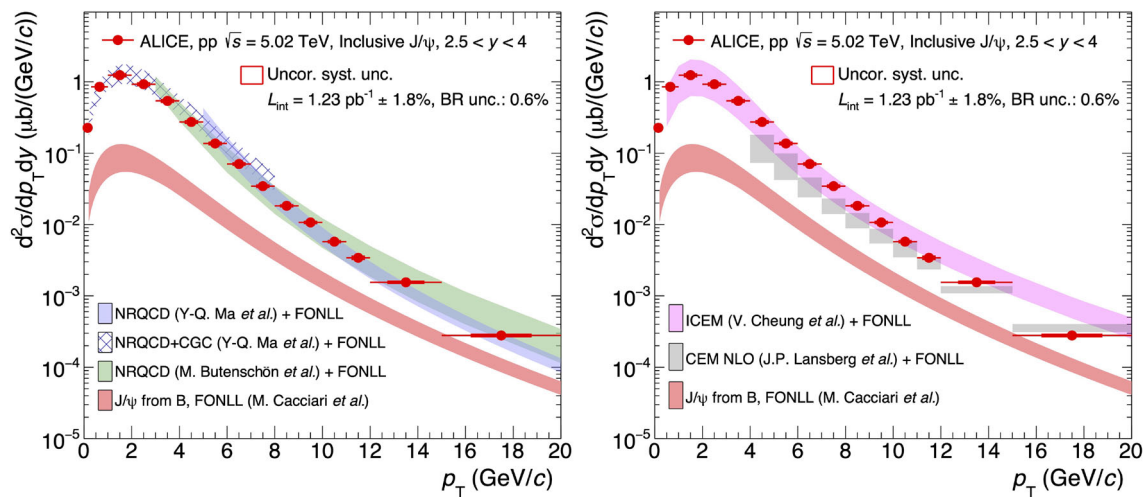
Fig. 2 Transverse momentum dependence of the inclusive J/ψ cross section. The measurements are compared to theoretical calculations from Refs. [44–46] (left) and Refs. [47–49] (right). The calculations of the non-prompt contribution [49] are also shown separately. See text for details
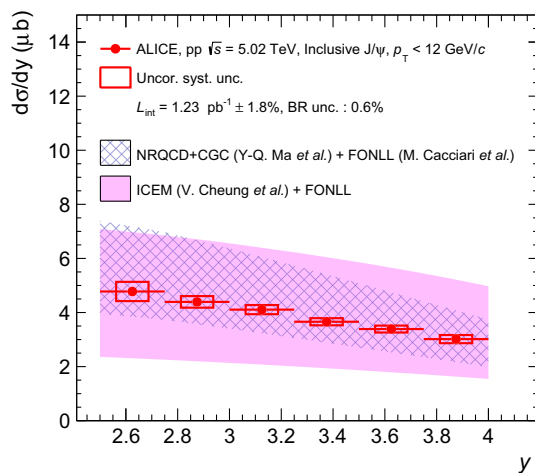
Fig. 3 Rapidity dependence of the inclusive J/ψ cross section. The measurements are compared to theoretical calculations from Refs. [46, 47]

4.1 Charmonium production

4.1.1 J/ψ cross section

The inclusive J/ψ production cross section in pp collisions at $\sqrt{s} = 5.02$ TeV integrated over $2.5 < y < 4$ and $p_{\rm T} < 20$ GeV/c is $\sigma_{J/\psi} = 5.88 \pm 0.03$ (stat.) ± 0.34 (syst.) μb. The differential cross sections are shown as a function of $p_{\rm T}$ and y in Figs. 2 and 3, respectively. The results are in agreement with the previously published ALICE measurements [8,9]. A maximum deviation of 1.8σ for $4 < p_{\rm T} < 5$ GeV/c and $3.75 < y < 4$ is found, where the comparison is performed using the quantity $\sigma_{J/\psi} \times$ BR in order to remove the BR uncertainty. These new measurements extend the $p_{\rm T}$ reach from 12 GeV/c to 20 GeV/c. The cross sections are in agreement, within uncertainties, with the recent LHCb results [10]. The

inclusive J/ψ double-differential production cross section is shown as a function of y for various $p_{\rm T}$ ranges in the four panels of Fig. 4. These measurements will also serve as reference for studying the nuclear modification of J/ψ production in Pb–Pb collisions. To this purpose, for the $p_{\rm T}$ and y double-differential pp cross sections, J/ψ with $p_{\rm T} < 0.3$ GeV/c were excluded to match a similar selection applied in Pb–Pb collisions to remove the photoproduction contribution, occurring besides the hadronic one, and relevant at low $p_{\rm T}$ in peripheral collisions [43].

The cross sections are compared with three theoretical calculations based on NRQCD: two Next-to-Leading Order (NLO) NRQCD calculations from Butenschön et al. [44] and from Ma et al. [45], and a Leading Order (LO) NRQCD calculation coupled to a Color Glass Condensate (CGC) description of the proton structure for low-x gluons from Ma et al. [46], labelled as NRQCD+CGC in the following. They are also compared to two theoretical calculations based on CEM: an improved CEM (ICEM) calculation from Cheung et al. [47] and a NLO CEM calculation from Lansberg et al. [48]. While the NLO calculations presented here are not reliable in the low-$p_{\rm T}$ region ($p_{\rm T} \lesssim M_{c\bar{c}}$), the calculations from NRQCD+CGC [46] or the semi-hard approach based on $k_{\rm T}$ factorization of the ICEM model [47] are available also at low $p_{\rm T}$. The theoretical calculations are for prompt J/ψ and account therefore for the decay of $\psi(2S)$ and χ_c into J/ψ. Since the measurements include as well non-prompt J/ψ, their contribution is estimated from Fixed-Order Next-to-Leading Logarithm (FONLL) calculations from Cacciari et al. [49]. The prompt and non-prompt J/ψ calculations are summed in order to obtain inclusive J/ψ calculations to be compared to the measurements. The uncertainties from renormalization and factorization scale and parton distribu-

tion function on prompt and non-prompt J/ψ production are considered as uncorrelated.

In Figs. 2, 3, and 4 the data are compared with the models described above when calculations are available. A good description of the p_T and y distributions of the data is obtained by the NRQCD models for $p_T > 3$ GeV/c for the model from Butenschön et al. and $p_T > 5$ GeV/c for the model from Ma et al.. The NRQCD+CGC model describes well the data as a function of p_T and y for $p_T < 8$ GeV/c. The ICEM model also gives a good description of the data as a function of y and p_T for $p_T < 15$ GeV/c. It overestimates the data for $p_T > 15$ GeV/c. Finally, the CEM NLO calculation underestimates the cross sections for $4 < p_T < 10$ GeV/c and reproduces the data at higher p_T. The nonprompt J/ψ contribution is also shown in Fig. 2, indicating that the contribution increases with increasing p_T from 7% at $p_T \approx 1$ GeV/c to 42% for the largest p_T interval.

4.1.2 $\psi(2S)$ cross section

The inclusive $\psi(2S)$ production cross section in pp collisions at $\sqrt{s} = 5.02$ TeV integrated over $p_T < 12$ GeV/c and for $2.5 < y < 4$ is $\sigma_{\psi(2S)} = 0.87 \pm 0.06$ (stat.) ± 0.10 (syst.) μb. The result is in agreement with the previously published $\psi(2S)$ cross section [9] and the deviation is found to be 0.75σ for the quantity $\sigma_{\psi}(2S) \times$ BR. An improvement of a factor $\sim$3 for the statistical uncertainty is obtained for the most recent data set. The first results on the p_T and y dependence of the inclusive $\psi(2S)$ cross section for $2.5 < y < 4$ in pp collisions at $\sqrt{s} = 5.02$ TeV are shown in Figs. 5 and 6, respectively.

Calculations of the same theory models as discussed in Sect. 4.1.1 are compared with the inclusive $\psi(2S)$ cross section in Figs. 5 and 6. As for the J/ψ case, the experimental measurements include a prompt and a non-prompt contribution while the model calculations are performed for the former only. Therefore, the $\psi(2S)$ non-prompt contribution,
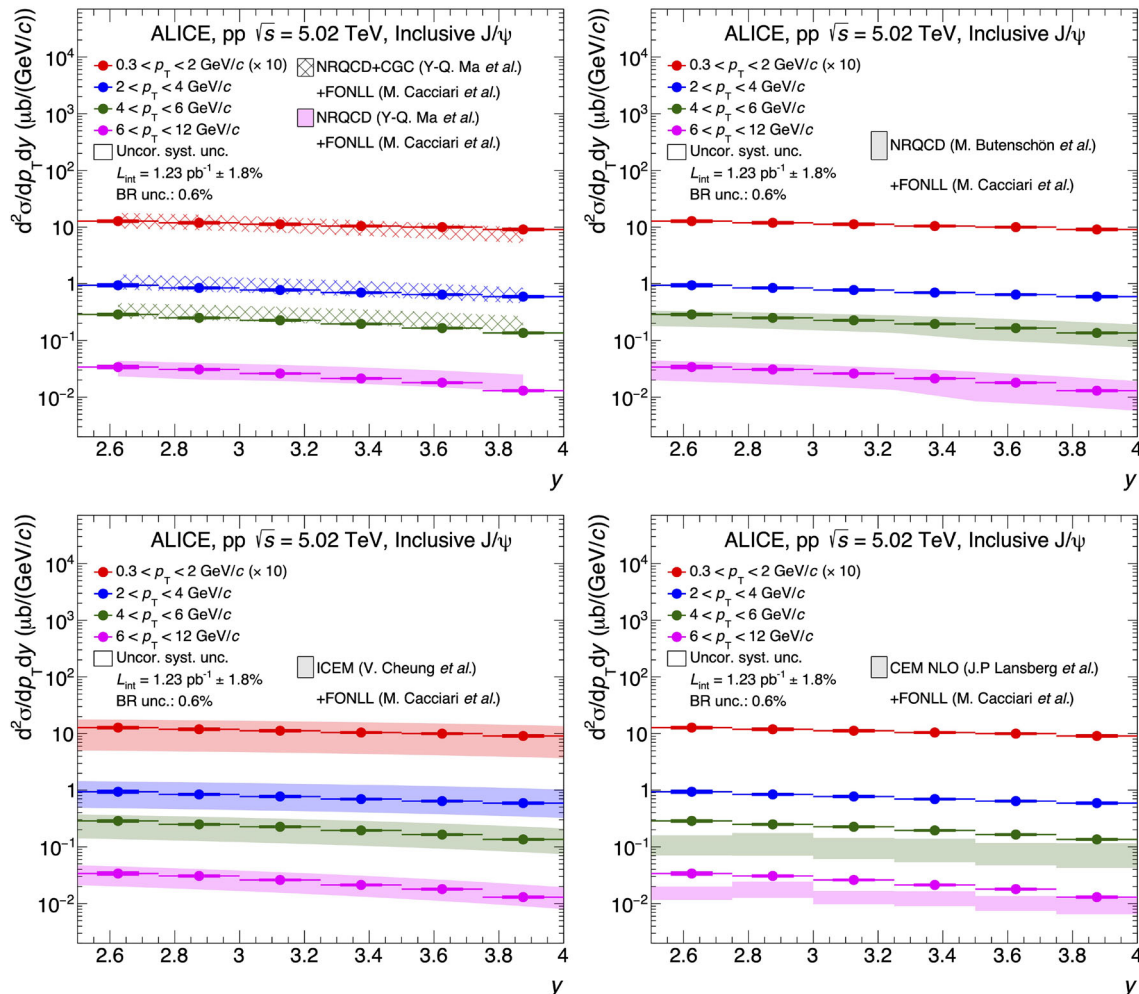
Fig. 4 Rapidity dependence of the inclusive J/ψ cross section for various p_T ranges, compared to theoretical calculations [44–49]. The theoretical calculations are scaled as for the data for $0.3 < p_T < 2$ GeV/c. See text for details
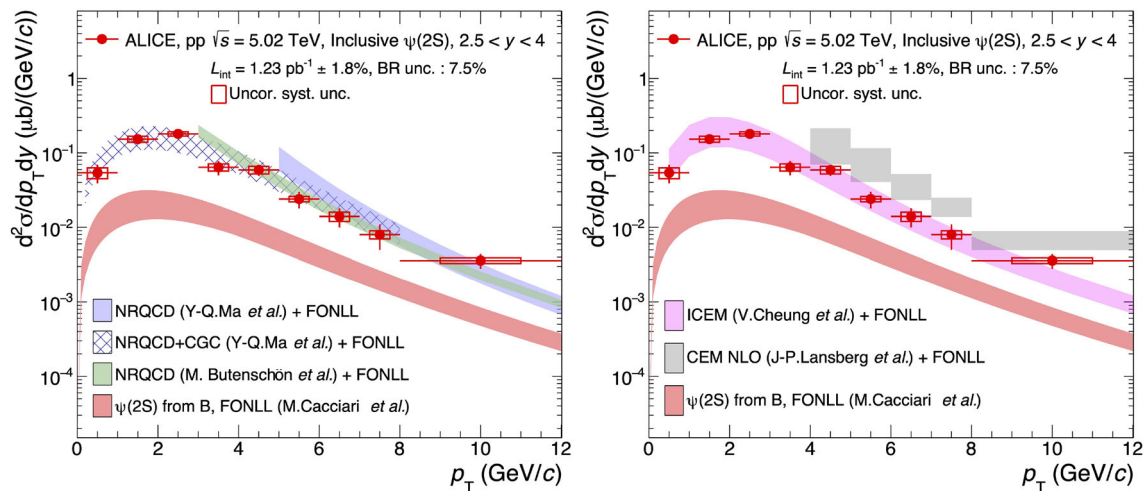
Fig. 5 The left and right panels show the p_T dependence for the inclusive $\psi(2S)$ production cross section in pp collisions at $\sqrt{s} = 5.02$ TeV. The results are compared with the theory predictions based on NRQCD [44–46] (left) and CEM [47,48] (right) models. The calculation of the non-prompt contribution from FONLL calculations [49] are also shown separately. See text for details
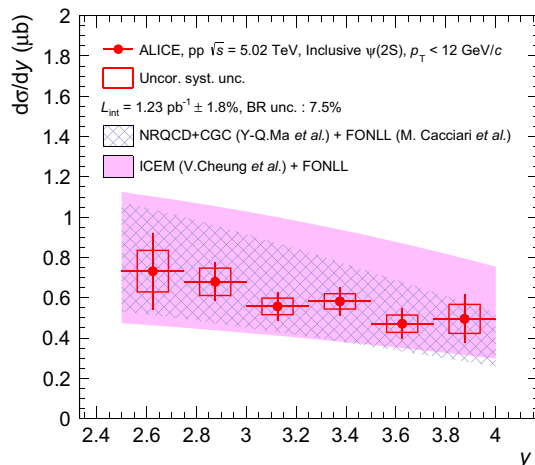
Fig. 6 Rapidity dependence for the inclusive $\psi(2S)$ production cross section in pp collisions at $\sqrt{s} = 5.02$ TeV. The results are compared with the theory predictions based on NRQCD+CGC [46] and ICEM [47] models. See text for details

according to FONLL [49], is summed to all theoretical predictions.

In the left panel of Fig. 5, the NRQCD calculation from Butenschön et al. [44] agrees with the experimental data for $4 < p_T < 12$ GeV/c, and the NRQCD calculation from Ma et al. [45] describes well the data except for $5 < p_T < 6$ GeV/c, where it overpredicts them. In addition, in the right panel of Fig. 5 there are significant deviations between the CEM NLO calculation [48] and the data at $p_T > 5$ GeV/c. The NRQCD+CGC [46] and ICEM [47] models provide a good description of the $\psi(2S)$ cross section as a function of p_T and y, albeit with large uncertainties for the y dependence, as it can be seen in Figs. 5 and 6, respectively. Finally, the

non-prompt $\psi(2S)$ contribution from FONLL [49] is also shown in Fig. 5 and varies from 10% to 25% as a function of p_T.

4.1.3 $\psi(2S)$ over J/ψ cross section ratio

The ratio between the inclusive $\psi(2S)$ and inclusive J/ψ production cross sections integrated over $p_T < 12$ GeV/c and for $2.5 < y < 4$, is 0.15 ± 0.01 (stat.) ± 0.02 (syst.). In Fig. 7, the p_T and y dependence of the $\psi(2S)$-to-J/ψ cross section ratio in pp collisions at $\sqrt{s} = 5.02$ TeV are shown in the left and right panel, respectively. The boxes represent the uncorrelated systematic uncertainties due to the MC input shapes and the signal extraction. The branching-ratio uncertainties, fully correlated versus p_T and y, are reported in the legend of Fig. 7. All the other systematic uncertainties are correlated over the two resonances and cancel out in the ratio.

The $\psi(2S)$-to-J/ψ production cross section ratio is also compared with theoretical models. As in previous sections, the non-prompt contribution from FONLL [49] is added to all theoretical calculations. Each individual source of theoretical uncertainty is considered as correlated among the two states and partially cancel in the ratio calculation. The NRQCD calculations from Butenschön et al. [44] describe well the p_T dependence of the cross section ratio within the large model uncertainties. A good description of the trend of the $\psi(2S)$-to-J/ψ cross section ratio as a function of p_T and y is also provided by the ICEM model [47]. In the left and right panels of Fig. 7, the non-prompt cross section ratios from FONLL [49] are also shown separately for completeness.
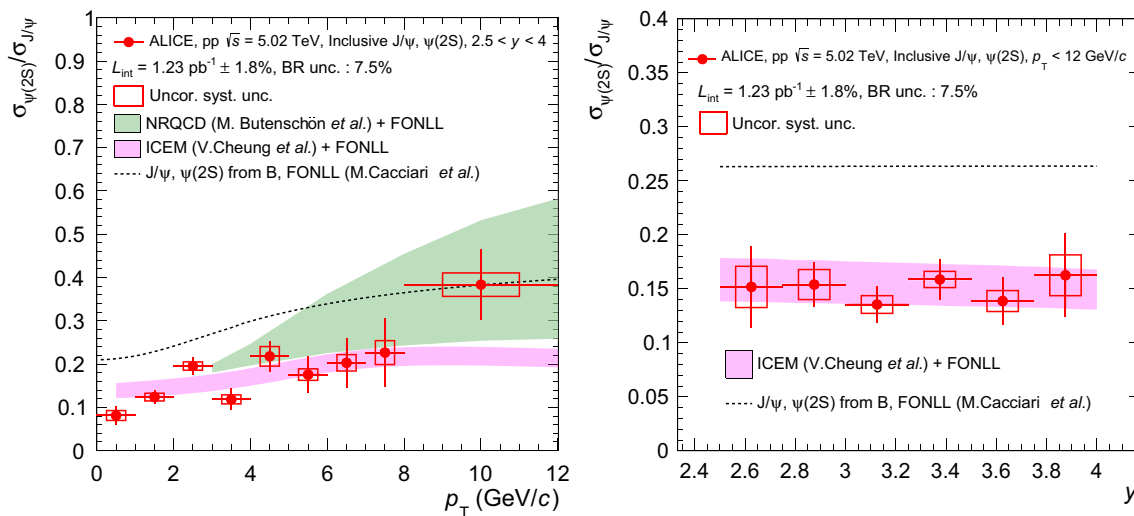
Fig. 7 The inclusive $\psi(2S)$-to-J/ψ cross section ratio as a function of p_T (left) and y (right), compared with theoretical calculations [44,47,49]. See text for details

4.2 Bottomonium production

The inclusive production cross sections of the three Υ states are measured for the first time in pp collisions at $\sqrt{s} = 5.02$ TeV and for $2.5 < y < 4$. The cross sections, integrated over $p_T < 15$ GeV/c and for $2.5 < y < 4$, are:

- $\sigma_{\Upsilon(1S)} = 45.5 \pm 3.9$ (stat.) ± 3.5 (syst.) nb,
- $\sigma_{\Upsilon(2S)} = 22.4 \pm 3.2$ (stat.) ± 2.7 (syst.) nb,
- $\sigma_{\Upsilon(3S)} = 4.9 \pm 2.2$ (stat.) ± 1.0 (syst.) nb.

The corresponding excited to ground-state ratios amount to:

- $\sigma_{\Upsilon(2S)}/\sigma_{\Upsilon(1S)} = 0.50 \pm 0.08$ (stat.) ± 0.06 (syst.),

- $\sigma_{\Upsilon(3S)}/\sigma_{\Upsilon(1S)} = 0.10 \pm 0.05$ (stat.) ± 0.02 (syst.).

The cross sections are presented in Fig. 8 as a function of p_T for the $\Upsilon(1S)$ on the left panel and as a function of y for the three Υ states, together with the CMS measurements [50].

The experimental results are compared to ICEM calculations [51] as well as to CEM NLO calculations [48]. Both approaches account for the feed-down contributions from heavier bottomonium states. The two CEM calculations describe the measured p_T-differential cross section within uncertainties. The y dependence shows that the forward ALICE acceptance covers the region where the production drops from the midrapidity plateau. This observation is in line
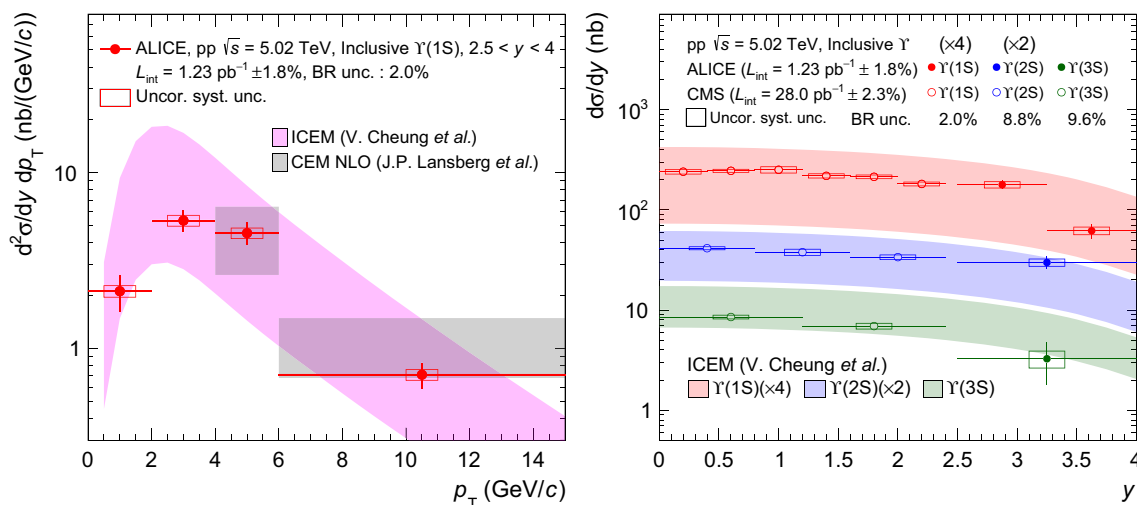
Fig. 8 Transverse momentum dependence of the $\Upsilon(1S)$ cross section (left) and y dependence of the $\Upsilon(1S)$, $\Upsilon(2S)$, and $\Upsilon(3S)$ (right) measured by ALICE and CMS. The two panels also show theoretical calculations [48,51]. See text for details

with the ICEM expectations. The measured $\Upsilon(2S)$ production cross section lies in the higher limit of the model while the $\Upsilon(3S)$ result lies at the lower edge of the theory band.

4.3 Energy dependence of quarkonium production

In Figs. 9 and 10 (left), the J/ψ p_T- and y-differential cross sections measured at $\sqrt{s} = 5.02$ TeV are compared with previous ALICE measurements at $\sqrt{s} = 7$ [12], 8 [13], and 13 TeV [9]. The ratio of the measurements at 5.02, 7, and 8 TeV to the 13 TeV results are also reported as a function of p_T at the bottom of Fig. 9 and as a function of y at the bottom of the left panel of Fig. 10. In Fig. 9 (and similarly in Fig. 11 for the $\psi(2S)$), in order to compute the ratios, the cross sections in some p_T intervals had to be merged. In the merged p_T intervals, the statistical uncertainty is the quadratic sum of the statistical uncertainties in each p_T interval, while the systematic uncertainty is the linear sum of the systematic uncertainties in each p_T interval to conservatively account for possible correlations. In Figs. 9, 10 (left), (and similarly in Figs. 10 (right) and 11 for the $\psi(2S)$), the global systematic uncertainties quoted as text in the top panel contain the branching ratio and luminosity uncertainty for a given energy, while the global systematic uncertainty quoted as text in the bottom panel contains the combination of the luminosity uncertainties at the two corresponding energies.

Both the statistical and systematic uncertainties are assumed to be uncorrelated among different energies when computing the cross section ratios.

Thanks to the large data sample used in this analysis, similar integrated luminosities are now collected at 5.02, 7, and 8 TeV, allowing for a systematic comparison of the J/ψ [$\psi(2S)$] differential yields, up to a p_T of 20 GeV/c [12 GeV/c]. The J/ψ p_T- and y-differential cross section values increase, as expected, with increasing collision energy. A stronger hardening of the p_T spectra is observed in the collisions at 13 TeV with respect to the 5.02, 7, and 8 TeV data, as can be seen in the ratio displayed at the bottom of Fig. 9. This hardening can derive from the increase of the prompt J/ψ mean p_T with energy, as well as by the increasing contribution from non-prompt J/ψ at high p_T. According to FONLL calculations [49], the fraction of non-prompt J/ψ to the inclusive J/ψ yield, for $p_T > 12$ GeV/c, is about 31% at 5.02 TeV, 37% at 7 and 8 TeV, and 40% at 13 TeV. The central values of the 7-to-13 TeV ratio are closer to the 5.02-to-13 than the 8-to-13 TeV ratio at low p_T contrary to the expectation of a smooth increase of the cross section with energy.

The J/ψ p_T-differential cross sections are compared with the NRQCD theoretical calculations from Butenschön et al. [44] (left) and to ICEM calculations [47] (right). As in Sect. 4.1, a non-prompt contribution from FONLL [49] is
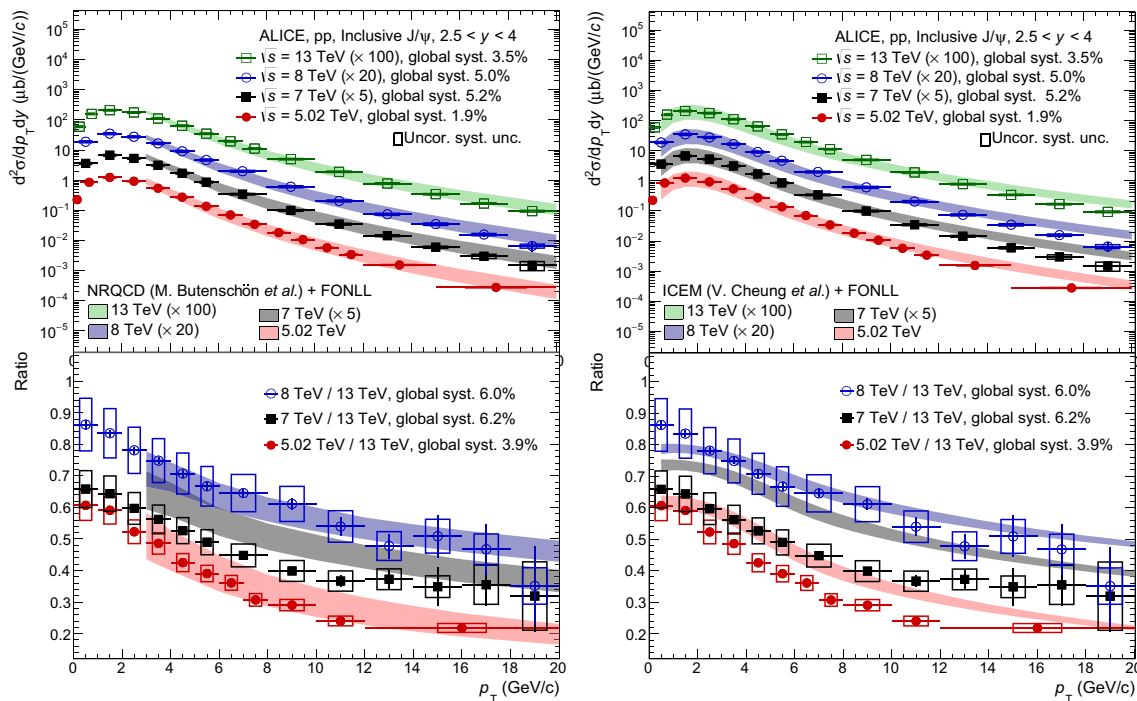
Fig. 9 Transverse momentum dependence of the inclusive J/ψ cross section, at forward y, measured in pp collisions at $\sqrt{s} = 5.02$, 7 [12], 8 [13], and 13 [9] TeV (top panels), and ratio of the measurements at 5.02, 7, and 8 TeV to the 13 TeV data (bottom panels). The data are compared with the NRQCD theoretical calculations from Butenschön et al. + FONLL (left panels) [44,49] and with theoretical calculations from ICEM + FONLL (right panels) [47,49]
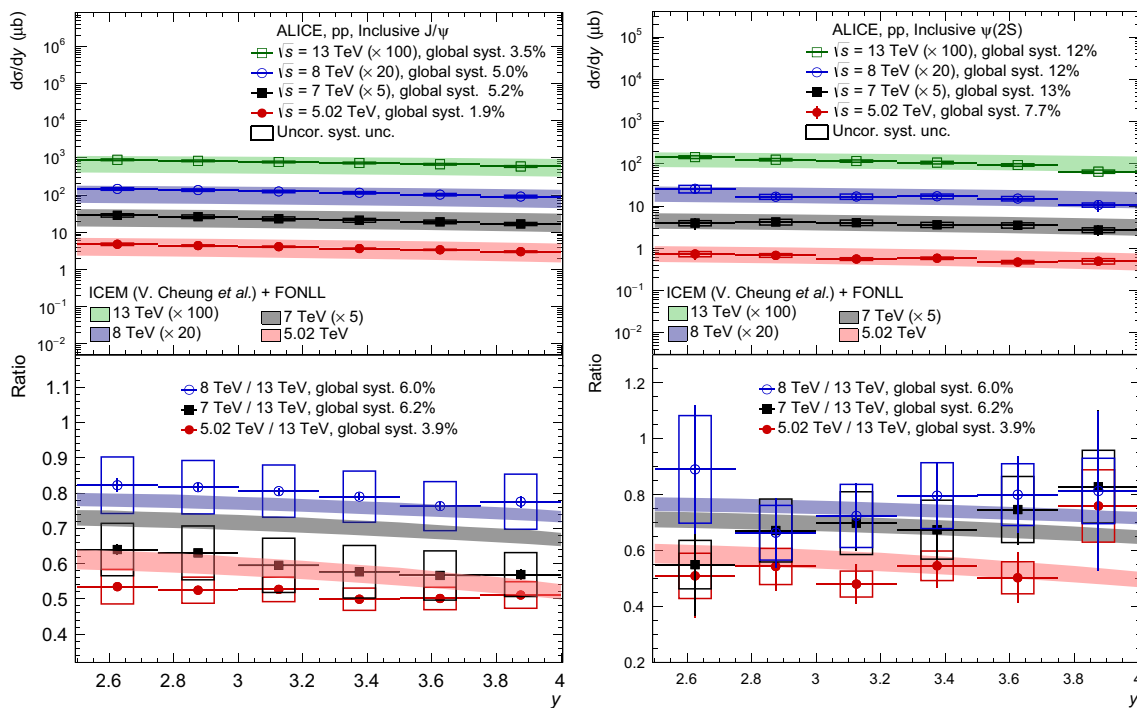
Fig. 10 Rapidity dependence of the inclusive J/ψ (left) and $\psi(2S)$ (right) cross section, at forward y, measured in pp collisions at $\sqrt{s} =$ 5.02, 7 [12], 8 [13], and 13 [9] TeV (top panels), and ratio of the measurements at 5.02, 7, and 8 TeV to the 13 TeV data (bottom panels). The data are compared with theoretical calculations from ICEM + FONLL [47,49]
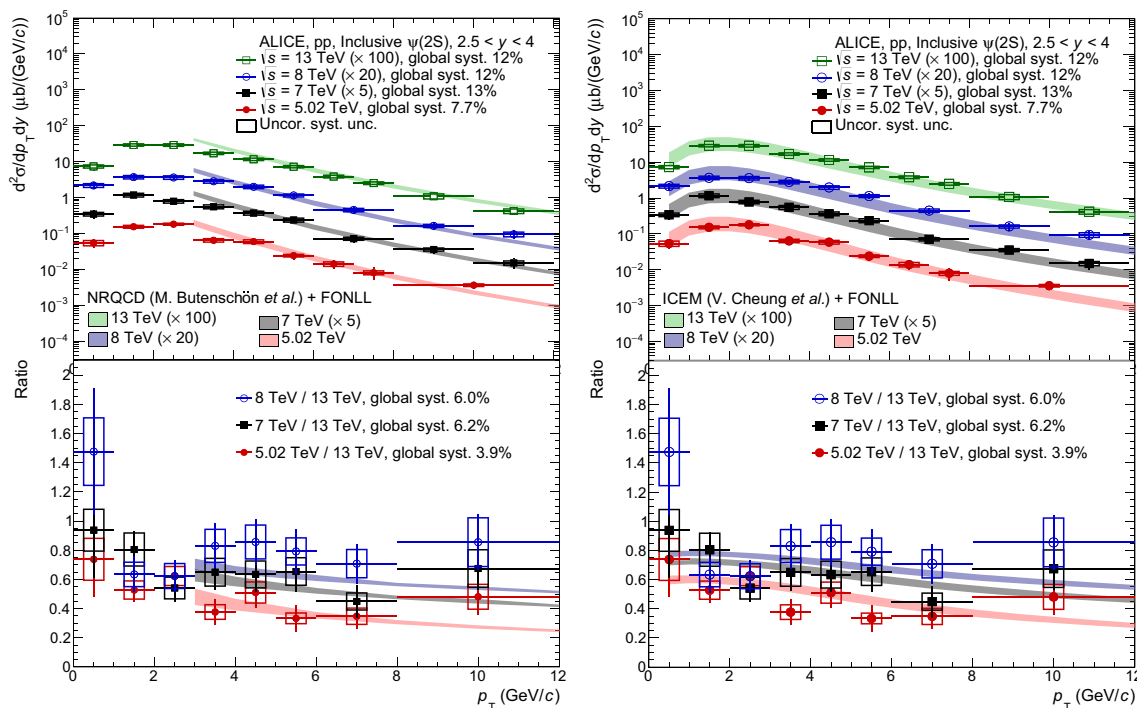
Fig. 11 Transverse momentum dependence of the inclusive $\psi(2S)$ cross section, at forward y, measured in pp collisions at $\sqrt{s} =$ 5.02, 7 [12], 8 [13], and 13 [9] TeV (top panels), and ratio of the measurements at 5.02, 7, 8 TeV to the 13 TeV data (bottom panels). The data are compared with the NRQCD theoretical calculations from Butenschön et al. + FONLL (left panels) [44,49] and with theoretical calculations from ICEM + FONLL (right panels) [47,49]
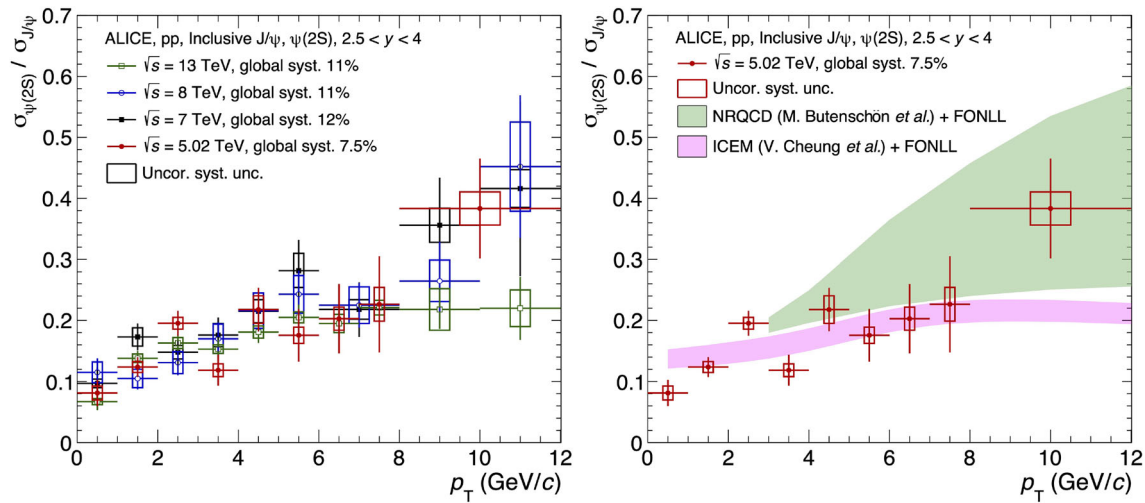
Fig. 12 Inclusive $\psi(2S)$-to-J/ψ cross section ratio as a function of p_T, at forward y, in pp collisions at $\sqrt{s}$ = 5.02, 7 [12], 8 [13], and 13 [9] TeV (left panel). The data at $\sqrt{s}$ = 5.02 TeV are compared with NRQCD theoretical calculations from Butenschön et al. + FONLL [44,49] and with theoretical calculations from ICEM + FONLL [47,49] (right panel)
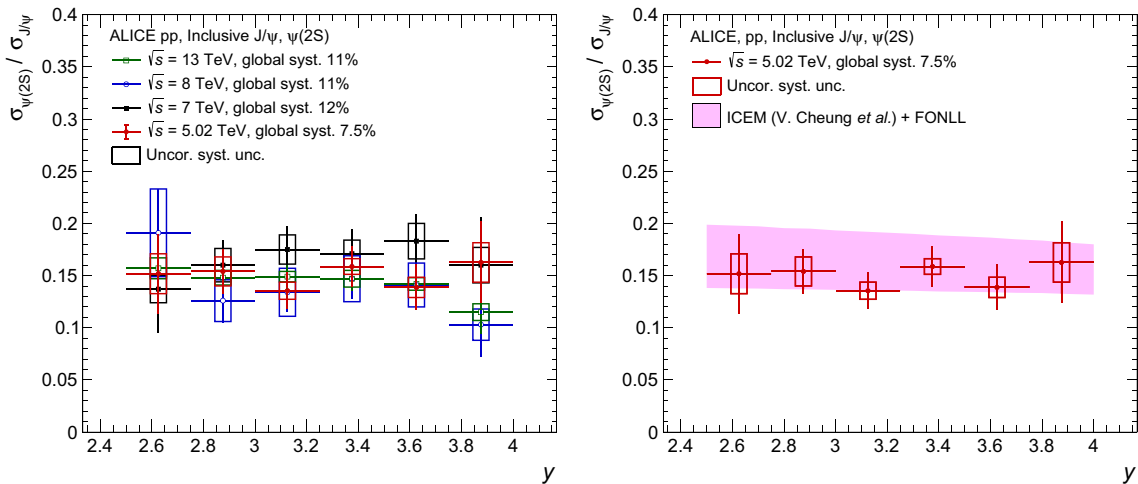
Fig. 13 Inclusive $\psi(2S)$-to-J/ψ cross section ratio as a function of y in pp collisions at $\sqrt{s}$ = 5.02, 7 [12], 8 [13], and 13 [9] TeV (left panel). The data at $\sqrt{s}$ = 5.02 TeV are compared with theoretical calculations from ICEM + FONLL [47,49] (right panel)

added to all the theoretical calculations for charmonium production. The agreement of both model calculations is rather good for all the energies and covered p_T ranges, although they both tend to slightly overestimate (or are at the upper edge of) the data at p_T > 12 GeV/c for ICEM and p_T > 16 GeV/c for NRQCD from Butenschön, and this is more pronounced for the ICEM computation. The charmonium p_T- and y-differential cross section ratios among different energies can provide stronger constraints on the theoretical models. Indeed, similarly as for the $\psi(2S)$-to-J/ψ ratio in Sect. 4.1.3, the individual uncertainty sources on prompt charmonium (charm mass, renormalization and factorization scale) and non-prompt charmonium (bottom mass, renormalization and factorization scale, and parton distribution function) are con-

sidered as correlated among the considered energies and partially cancel in the ratio calculation. On the bottom panels of Fig. 9, the ratios are compared with theoretical calculations from NRQCD from Butenschön et al. [44] (left) and ICEM [47] (right) calculations. The NRQCD calculation is able to successfully describe the 5.02-to-13 TeV and 8-to-13 TeV ratios in the whole p_T range of validity of the model, while it slightly overestimates, or is at the upper edge of data, for the 7-to-13 TeV ratio. The ICEM calculation can only satisfactorily describe the 8-to-13 TeV ratio, while the model calculation is systematically above the 5.02-to-13 and the 7-to-13 TeV data, except in the very-low- and very-high-p_T region.

In the left panel of Fig. 10, the J/ψ y-differential cross section shows a slight decrease with increasing y at all energies. The ratio of the lower energy data to the 13 TeV data exhibits a flat behaviour within the experimental uncertainties for the three energies. The y-differential cross sections and cross section ratios between the available energies are also compared to the ICEM model [47]. The model is able to reproduce the cross sections at all energies, as well as the decreasing trend with increasing y, but suffers from large theoretical uncertainties. Similarly to what is observed for the p_T-dependent cross section ratios, the ICEM calculation successfully describes the 8-to-13 TeV ratio over the entire y range, but overestimates, or is at the edges of the 5.02-to-13 and 7-to-13 TeV cross section ratios. The NRQCD model prediction from Butenschön et al. [44], being available only for $p_T > 3$ GeV/c, cannot be compared to the p_T-integrated cross section.

The ψ(2S) y-differential cross section is presented in the right panel of Fig. 10. The results at $\sqrt{s}$ = 13 TeV, similarly to the J/ψ ones, show a decreasing trend with increasing y, which is less evident at lower energy because of the larger statistical uncertainties. As shown in Fig. 10 (right), the 5.02-to-13, 7-to-13, and 8-to-13 TeV ratios display no strong y dependence within the experimental uncertainties. As for the J/ψ, the y-differential cross section ratios are compared to the ICEM calculation [47]. The cross sections and their y dependence are well reproduced by the model at the various energies. Within the large experimental uncertainties, the ICEM model is able to reproduce consistently the 5.02-to-13, 7-to-13, and 8-to-13 TeV ratios. The inclusive ψ(2S) p_T-differential cross sections measured at $\sqrt{s}$ = 5.02, 7, 8, and 13 TeV are compared in Fig. 11. The cross section increases with increasing collision energy. Contrary to the J/ψ case, the 5.02-to-13, 7-to-13, and 8-to-13 TeV ratios in the bottom panel of Fig. 11 exhibit a flat p_T dependence for $3 \leq p_T < 12$ GeV/c, indicating that no significant hardening of the p_T spectrum is seen, within the data uncertainties, at the highest collision energy with respect to the lower energies. The inclusive ψ(2S) p_T-differential cross section and cross section ratios among energies are also compared with the NRQCD calculation from Butenschön et al. [44] (left panel of Fig. 11) and with the ICEM model [47] (right panel of Fig. 11). Both models are able to satisfactorily describe the ψ(2S) p_T-differential cross section measurements at all the displayed energies. One can however remark that the NRQCD calculation overestimates systematically the cross sections for $3 \leq p_T < 4$ GeV/c, and that both the NRQCD and ICEM models are at the lower edges of the measurements for $p_T \geq 8$ GeV/c and for $\sqrt{s}$ = 5.02, 7, and 8 TeV. Concerning the cross section ratios, the NRQCD model reproduces the 5.02-to-13 and 7-to-13 TeV data for $3 \leq p_T < 8$ GeV/c, and underestimates them for $p_T \geq 8$ GeV/c and in almost the whole

p_T range for the 8-to-13 TeV ratio. Similarly, the ICEM calculation describes successfully the trend versus p_T of the 5.02-to-13 and 7-to-13 TeV ratios for $p_T < 8$ GeV/c, and additionally it provides a reasonable description of the 8-to-13 TeV ratio for $2 \leq p_T < 8$ GeV/c, given the current experimental uncertainties. Both the NRQCD calculation and ICEM model suggest a weak hardening of the ψ(2S) p_T spectrum with the collision energy, which is not observed in data, possibly due to large experimental uncertainties.

The ψ(2S)-to-J/ψ cross section ratio is displayed as a function of p_T, y, and integrated over p_T and y for 2.5 < y < 4 for the different pp colliding energies in Figs. 12 (left), 13 (left), and 14 (left), respectively. The p_T-differential ψ(2S)-to-J/ψ ratio increases with increasing p_T and does not exhibit any energy dependence within the current uncertainties. Similarly, no significant change in shape nor in magnitude is observed in the y-dependent ψ(2S)-to-J/ψ cross section ratio, which follows a flat trend with y. The y and p_T-integrated ψ(2S)-to-J/ψ ratio for 2.5 < y < 4 is also compatible with no energy dependence within the measurement uncertainties. The ψ(2S)-to-J/ψ ratio as a function of p_T is also compared to the NRQCD from Butenschön et al. [44] and ICEM [47] models in the right panel of Fig. 12 for $\sqrt{s}$ = 5.02 TeV and in Fig. 15 of the appendix for $\sqrt{s}$ = 7, 8 and 13 TeV. In both models the ψ(2S)-to-J/ψ ratio does not exhibit a strong energy dependence, as in data. The NRQCD model describes within uncertainties the ψ(2S)-to-J/ψ ratio at 5.02, 7, and 8 TeV for $p_T \geq 3$ GeV/c, but it tends to overestimate it at 13 TeV, where the uncertainties are smaller. The ICEM calculation qualitatively describes the p_T dependence of the ψ(2S)-to-J/ψ ratio at the four energies for $p_T < 8$ GeV/c, and suggests a flat behaviour for $p_T \geq 8$ GeV/c in agreement with the 13 TeV data which are the most precise ones. In Fig. 13 right, the y-differential ψ(2S)-to-J/ψ cross section ratio at $\sqrt{s}$ = 5.02 TeV is compared with the ICEM calculation. Similar data to theory comparison can be found in Fig. 16 of the appendix for pp collisions at $\sqrt{s}$ = 7, 8 and 13 TeV. The model predicts a flat y dependence and properly describes the data at the four energies within the experimental and theoretical uncertainties.

The energy dependence of the ψ(2S)-to-J/ψ ratio integrated in p_T and y for 2.5 < y < 4 is also compared with the ICEM model in Fig. 14 (left). The charmonium cross section ratio does not exhibit a significant energy dependence and is well reproduced by the ICEM model. Finally, the cross section per unit of rapidity for 2.5 < y < 4 and integrated over p_T is displayed as a function of the collision energy in the right panel of Fig. 14, for all available ALICE quarkonium measurements. A steady increase of the cross section is observed with increasing $\sqrt{s}$ for all the states. ALICE data are compared with theoretical calculations from ICEM [47]. The model, within its large uncertainties, is able to consis-
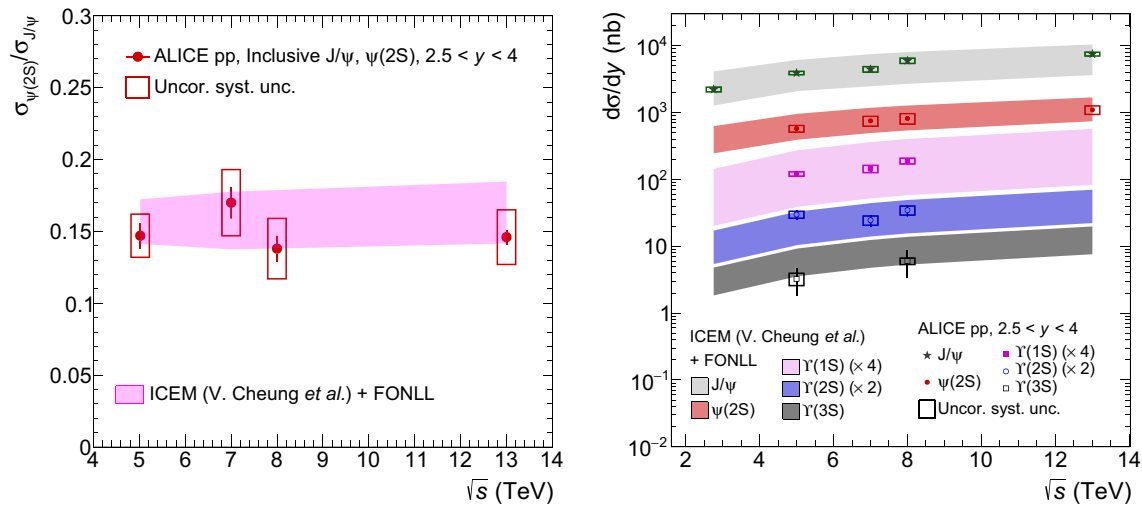
Fig. 14 Inclusive $\psi(2S)$-to-J/ψ cross section ratio (left) and J/ψ, $\psi(2S)$, $\Upsilon(1S)$, $\Upsilon(2S)$, and $\Upsilon(3S)$ p_T-integrated cross section per unit of rapidity (right) as a function of the collision energy in pp collisions [9,11–13]. In the left panel, the systematic boxes include the BR uncertainties from both resonances, on top of the MC input and signal extraction systematic uncertainties. The 13 TeV data point is computed from the published individual J/ψ and $\psi(2S)$ p_T-integrated cross sections. The statistical and systematic uncertainties are assumed to be uncorrelated between the resonances when computing the ratio. In the right panel, the luminosity and branching ratio uncertainties are included in the systematic boxes. The data are compared with theoretical calculations from ICEM + FONLL [47,49]

tently reproduce the energy dependence of the cross section for all the quarkonium states. However, the $\Upsilon(3S)$ results lie on the lower edge of the theoretical calculation band.

5 Conclusion

The inclusive production cross sections of J/ψ, $\psi(2S)$, $\Upsilon(1S)$, $\Upsilon(2S)$, and $\Upsilon(3S)$ have been measured with the ALICE detector at forward rapidity ($2.5 < y < 4$) in pp collisions at $\sqrt{s} = 5.02$ TeV. The J/ψ and $\psi(2S)$ results are in agreement with earlier measurements at the same energy. Thanks to the larger integrated luminosity by a factor 12 of these new measurements, a p_T reach up to 20 GeV/c has been achieved for the J/ψ, and the double-differential cross section as a function of p_T and y could also be extracted. The $\psi(2S)$ and $\Upsilon(1S)$ production cross section and the $\psi(2S)$-to-J/ψ cross section ratio have been measured for the first time as a function of p_T and y at forward rapidity, as well as the p_T-integrated $\Upsilon(1S)$, $\Upsilon(2S)$, and $\Upsilon(3S)$ cross sections. The collision energy dependence has been discussed for the five quarkonium states and the ratios of the cross sections at $\sqrt{s} = 5.02$, 7, and 8 TeV to the one obtained at $\sqrt{s} = 13$ TeV have been presented as a function of p_T and y. Calculations based on CEM or NRQCD describe well the charmonium and bottomonium cross sections at all collision energies, as well as the $\psi(2S)$-to-J/ψ ratio, in the kinematic range they cover. The charmonium cross sections and their ratios relative to the values at $\sqrt{s} = 13$ TeV can be described by a NRQCD model

within uncertainties. These combined measurements provide additional experimental constraints to quarkonium production models. This is particularly evident for the determination of the cross section calculations, where a reduction in the size of the theory should now be pursued in order to match the experimental precision. Moreover, the $\sqrt{s} = 5.02$ TeV pp measurements represent a more accurate reference for the measurement of the quarkonium nuclear modification factor in Pb–Pb collisions collected during the LHC Run 2 at the same nucleon–nucleon center-of-mass energy.

Data Availability Statement This manuscript has associated data in a data repository. [Authors' comment: Manuscript has associated data in a HEPData repository at https://www.hepdata.net/.]

A Appendix

The $\psi(2S)$-to-J/ψ cross section ratio is displayed as a function of p_T for pp collisions at $\sqrt{s}$ = 7 [12], 8 [13] and 13 TeV [9] in the top left, top right, and bottom left panel of Fig. 15, respectively. It is compared to the NRQCD model from Butenschön et al. [44] and to the ICEM [47] model, as in Fig. 12 right for the results obtained at $\sqrt{s}$ = 5.02 TeV.

The $\psi(2S)$-to-J/ψ cross section ratio is displayed as a function of y for pp collisions at $\sqrt{s}$ = 7 [12], 8 [13] and 13 TeV [9] in the top left, top right, and bottom left panel of Fig. 16, respectively. It is compared with the ICEM [47] calculation, as in Fig. 13 right for the results obtained at $\sqrt{s}$ = 5.02 TeV.
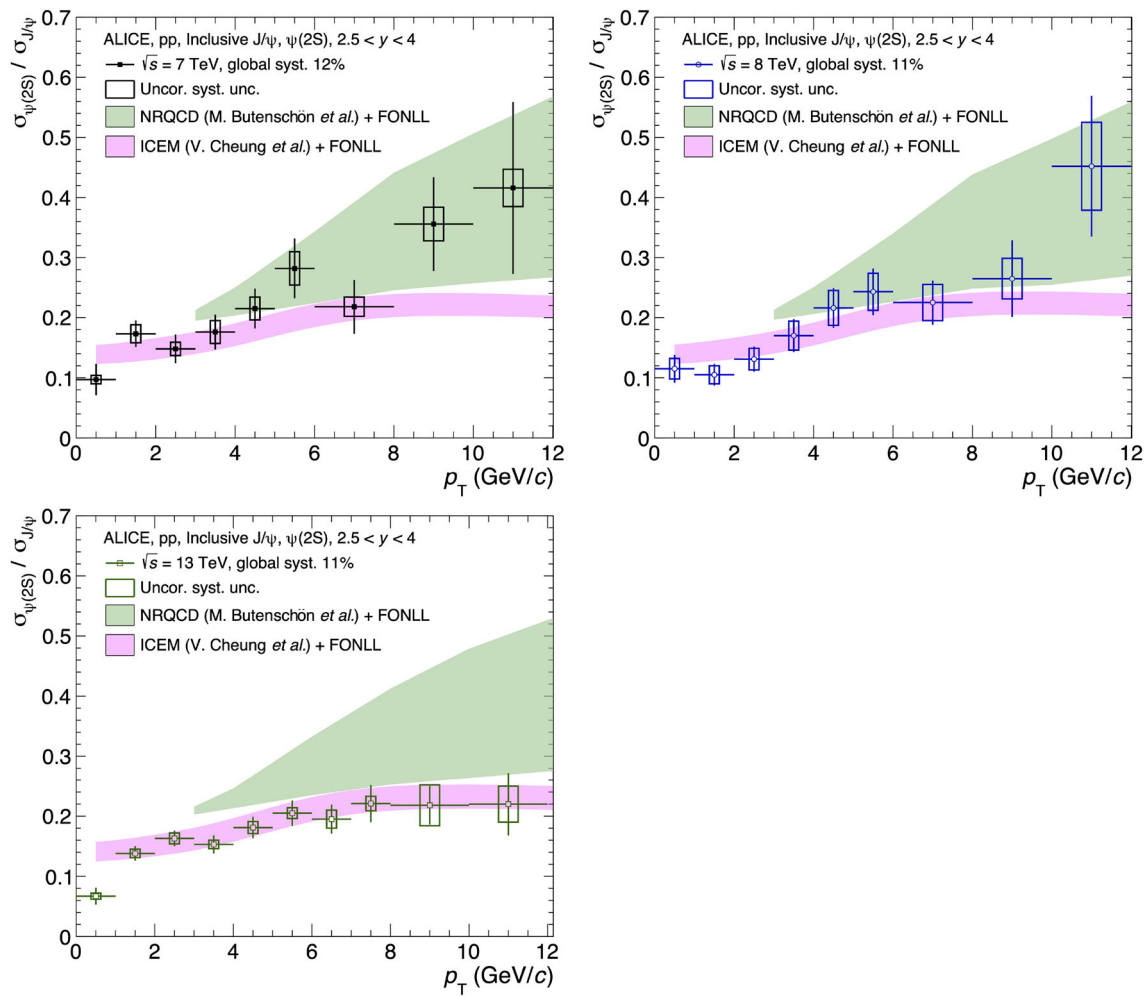
Fig. 15 Inclusive $\psi(2S)$-to-J/ψ cross section ratio as a function of p_{T}, at forward y, in pp collisions at $\sqrt{s}=7$ [12] (top left), 8 [13] (top right), and 13 TeV [9] (bottom left). The data are compared with NRQCD theoretical calculations from Butenschön et al. + FONLL [44,49] and with theoretical calculations from ICEM + FONLL [47,49]
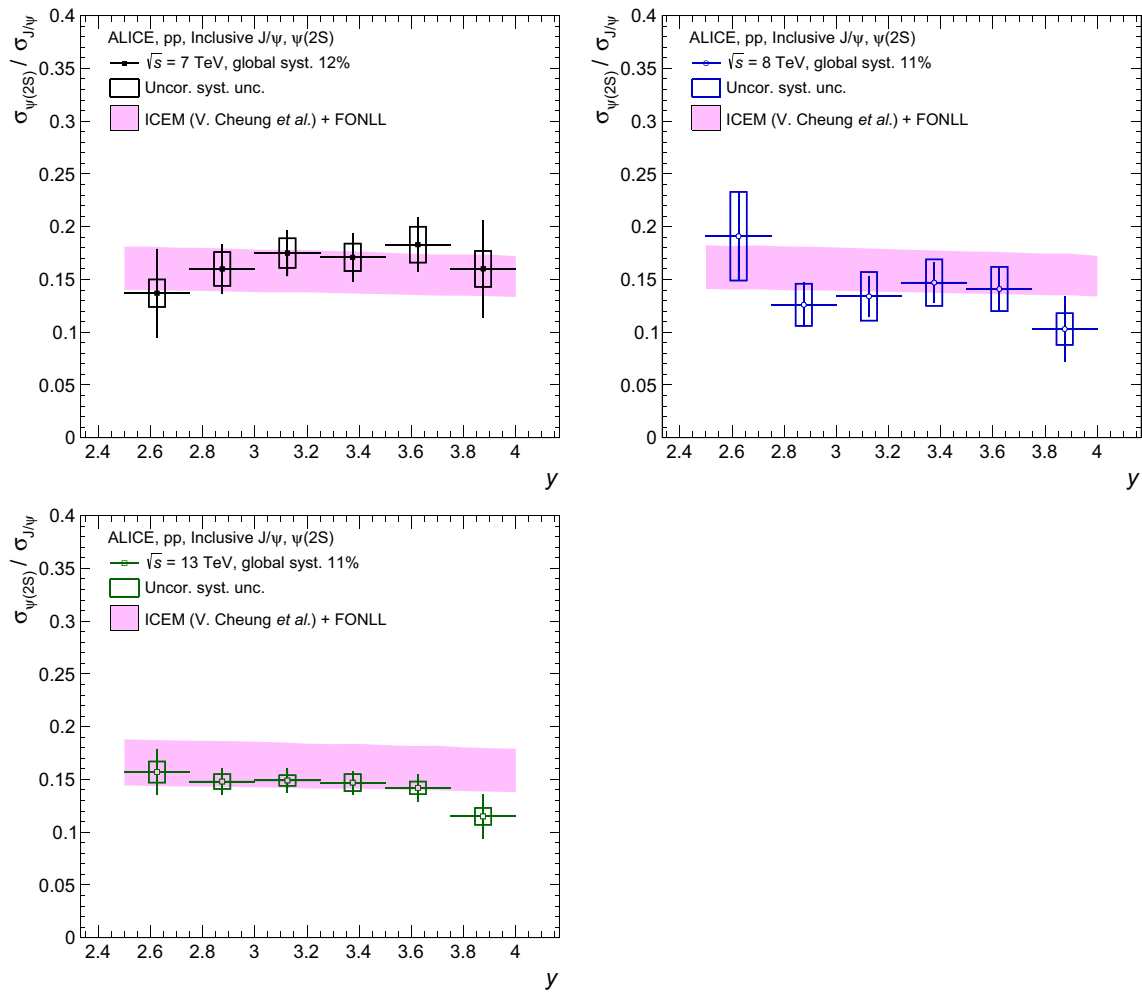
Fig. 16 Inclusive $\psi(2S)$-to-J/ψ cross section ratio as a function of y in pp collisions at $\sqrt{s}$ = 7 [12] (top left), 8 [13] (top right), and 13 TeV [9] (bottom left). The data are compared with theoretical calculations from ICEM + FONLL [47,49]

References

1. N. Brambilla et al., Heavy quarkonium: progress, puzzles, and opportunities. Eur. Phys. J. C **71**, 1534 (2011). https://doi.org/10.1140/epjc/s10052-010-1534-9. arXiv:1010.5827 [hep-ph]
2. A. Andronic et al., Heavy-flavour and quarkonium production in the LHC era: from proton–proton to heavy-ion collisions. Eur. Phys. J. C **76**(3), 107 (2016). https://doi.org/10.1140/epjc/s10052-015-3819-5. arXiv:1506.03981 [nucl-ex]
3. A. Rothkopf, Heavy quarkonium in extreme conditions. Phys. Rep. **858**, 1–117 (2020). https://doi.org/10.1016/j.physrep.2020.02.006. arXiv:1912.02253 [hep-ph]
4. H. Fritzsch, Producing heavy quark flavors in hadronic collisions: a test of quantum chromodynamics. Phys. Lett. B **67**, 217–221 (1977). https://doi.org/10.1016/0370-2693(77)90108-3
5. J. Amundson, O.J. Eboli, E. Gregores, F. Halzen, Quantitative tests of color evaporation: charmonium production. Phys. Lett. B **390**, 323–328 (1997). https://doi.org/10.1016/S0370-2693(96)01417-7. arXiv:hep-ph/9605295
6. R. Baier, R. Ruckl, Hadronic production of J/psi and upsilon: transverse momentum distributions. Phys. Lett. B **102**, 364–370 (1981). https://doi.org/10.1016/0370-2693(81)90636-5
7. G.T. Bodwin, E. Braaten, G. Lepage, Rigorous QCD analysis of inclusive annihilation and production of heavy quarkonium. Phys. Rev. D **51** 1125–1171 (1995) [Erratum: Phys. Rev. D 55, 5853 (1997)]. https://doi.org/10.1103/PhysRevD.55.5853. arXiv:hep-ph/9407339
8. ALICE Collaboration, J. Adam et al., J/ψ suppression at forward rapidity in Pb-Pb collisions at $\sqrt{s_{NN}}$ = 5.02 TeV. Phys. Lett. B **766**, 212–224 (2017). https://doi.org/10.1016/j.physletb.2016.12.064. arXiv:1606.08197 [nucl-ex]
9. ALICE Collaboration, S. Acharya et al., Energy dependence of forward-rapidity J/ψ and $\psi(2S)$ production in pp collisions at the LHC. Eur. Phys. J. C **77**(6), 392 (2017). https://doi.org/10.1140/epjc/s10052-017-4940-4. arXiv:1702.00557 [hep-ex]
10. LHCb Collaboration, R. Aaij et al., Measurement of J/ψ production cross-sections in pp collisions at $\sqrt{s}$ = 5 TeV. arXiv:2109.00220 [hep-ex]
11. ALICE Collaboration, B. Abelev et al., Inclusive J/ψ production in pp collisions at $\sqrt{s}$ = 2.76 TeV. Phys. Lett. B **718**, 295–306 (2012) [Erratum: Phys. Lett. B 748, 472 (2015)]. https://doi.org/10.1016/j.physletb.2012.10.078. arXiv:1203.3641 [hep-ex]
12. ALICE Collaboration, B. Abelev et al., Measurement of quarkonium production at forward rapidity in pp collisions at $\sqrt{s}$ = 7 TeV. Eur. Phys. J. C **74**(8), 2974 (2014). https://doi.org/10.1140/epjc/s10052-014-2974-4. arXiv:1403.3648 [nucl-ex]
13. ALICE Collaboration, J. Adam et al., Inclusive quarkonium production at forward rapidity in pp collisions at $\sqrt{s}$ = 8 TeV. Eur. Phys. J. C **76**(4), 184 (2016). https://doi.org/10.1140/epjc/s10052-016-3987-y. arXiv:1509.08258 [hep-ex]
14. LHCb Collaboration, R. Aaij et al., Measurement of Upsilon production in pp collisions at $\sqrt{s}$ = 7 TeV. Eur. Phys. J. C **72**, 2025 (2012). https://doi.org/10.1140/epjc/s10052-012-2025-y. arXiv:1202.6579 [hep-ex]
15. LHCb Collaboration, R. Aaij et al., Production of J/psi and Upsilon mesons in pp collisions at sqrt(s) = 8 TeV. JHEP **06**, 064 (2013). https://doi.org/10.1007/JHEP06(2013)064. arXiv:1304.6977 [hep-ex]
16. LHCb Collaboration, R. Aaij et al., Forward production of Υ mesons in pp collisions at $\sqrt{s}$ = 7 and 8 TeV. JHEP **11**, 103 (2015). https://doi.org/10.1007/JHEP11(2015)103. arXiv:1509.02372 [hep-ex]
17. LHCb Collaboration, R. Aaij et al., Measurement of forward J/ψ production cross-sections in pp collisions at $\sqrt{s}$ = 13 TeV. JHEP **10**, 172 (2015) [Erratum: JHEP 05, 063 (2017)]. https://doi.org/10.1007/JHEP10(2015)172. arXiv:1509.00771 [hep-ex]
18. ALICE Collaboration, K. Aamodt et al., The ALICE experiment at the CERN LHC. JINST **3**, S08002 (2008). https://doi.org/10.1088/1748-0221/3/08/S08002
19. ALICE Collaboration, B. Abelev et al., Performance of the ALICE experiment at the CERN LHC. Int. J. Mod. Phys. A **29**, 1430044 (2014). https://doi.org/10.1142/S0217751X14300440. arXiv:1402.4476 [nucl-ex]
20. ALICE Collaboration, ALICE dimuon forward spectrometer: Technical Design Report, CERN-LHCC-99-022. http://cds.cern.ch/record/401974
21. ALICE Collaboration, K. Aamodt et al., Alignment of the ALICE inner tracking system with cosmic-ray tracks. JINST **5**, P03003 (2010). https://doi.org/10.1088/1748-0221/5/03/P03003. arXiv:1001.0502 [physics.ins-det]
22. M. Bondila et al., ALICE T0 detector. IEEE Trans. Nucl. Sci. **52**, 1705–1711 (2005). https://doi.org/10.1109/TNS.2005.856900
23. ALICE Collaboration, E. Abbas et al., Performance of the ALICE VZERO system. JINST **8**, P10016 (2013). https://doi.org/10.1088/1748-0221/8/10/P10016. arXiv:1306.3130 [nucl-ex]
24. ALICE Collaboration, ALICE 2017 luminosity determination for pp collisions at $\sqrt{s}$ = 5 TeV, ALICE-PUBLIC-2018-014. http://cds.cern.ch/record/2648933
25. S. van der Meer, Calibration of the Effective Beam Height in the ISR, CERN-ISR-PO-68-31. https://cds.cern.ch/record/296752
26. ALICE Collaboration, J. Adam et al., Centrality dependence of inclusive J/ψ production in p-Pb collisions at $\sqrt{s_{NN}}$ = 5.02 TeV. JHEP **11**, 127 (2015). https://doi.org/10.1007/JHEP11(2015)127. arXiv:1506.08808 [nucl-ex]
27. ALICE Collaboration, B. Abelev et al., Heavy flavour decay muon production at forward rapidity in proton–proton collisions at $\sqrt{s}$ = 7 TeV. Phys. Lett. B **708**, 265–275 (2012). https://doi.org/10.1016/j.physletb.2012.01.063. arXiv:1201.3791 [hep-ex]
28. ALICE Collaboration, Quarkonium signal extraction in ALICE, ALICE-PUBLIC-2015-006. https://cds.cern.ch/record/2060096
29. Particle Data Group Collaboration, P.A. Zyla et al., Review of particle physics. PTEP **2020**(8), 083C01 (2020). https://doi.org/10.1093/ptep/ptaa104
30. R. Brun, F. Bruyant, F. Carminati, S. Giani, M. Maire, A. McPherson, G. Patrick, L. Urban, GEANT: Detector Description and Simulation Tool; Oct 1994. CERN Program Library. CERN, Geneva (1993). Long Writeup W5013. https://doi.org/10.17181/CERN.MUHF.DMJ1. https://cds.cern.ch/record/1082634
31. GEANT4 Collaboration, S. Agostinelli et al., GEANT4: a simulation toolkit. Nucl. Instrum. Methods A **506**, 250–303 (2003). https://doi.org/10.1016/S0168-9002(03)01368-8
32. F. Bossú, Z. Conesa del Valle, A. de Falco, M. Gagliardi, S. Grigoryan, G. Martinez Garcia, Phenomenological interpolation of the inclusive J/psi cross section to proton–proton collisions at 2.76 TeV and 5.5 TeV. arXiv:1103.2394 [nucl-ex]
33. ALICE Collaboration, S. Acharya et al., Measurement of the inclusive J/ψ polarization at forward rapidity in pp collisions at $\sqrt{s}$ = 8 TeV. Eur. Phys. J. C **78**(7), 562 (2018). https://doi.org/10.1140/epjc/s10052-018-6027-2. arXiv:1805.04374 [hep-ex]
34. ALICE Collaboration, B. Abelev et al., J/ψ polarization in pp collisions at $\sqrt{s}$ = 7 TeV. Phys. Rev. Lett. **108**, 082001 (2012). https://doi.org/10.1103/PhysRevLett.108.082001. arXiv:1111.1630 [hep-ex]
35. LHCb Collaboration, R. Aaij et al., Measurement of J/ψ polarization in pp collisions at $\sqrt{s}$ = 7 TeV. Eur. Phys. J. C **73**(11), 2631 (2013). https://doi.org/10.1140/epjc/s10052-013-2631-3. arXiv:1307.6379 [hep-ex]
36. LHCb Collaboration, R. Aaij et al., Measurement of $\psi(2S)$ polarisation in pp collisions at $\sqrt{s}$ = 7 TeV. Eur. Phys. J. C **74**(5),

37. LHCb Collaboration, R. Aaij *et al.*, Measurement of the Υ polarizations in *pp* collisions at $\sqrt{s}$ = 7 and 8 TeV. JHEP **12**, 110 (2017). https://doi.org/10.1007/JHEP12(2017)110. arXiv:1709.01301 [hep-ex]

38. D. Lange, The EvtGen particle decay simulation package. Nucl. Instrum. Methods A **462**, 152–155 (2001). https://doi.org/10.1016/S0168-9002(01)00089-4

39. E. Barberio, B. van Eijk, Z. Was, PHOTOS: a universal Monte Carlo for QED radiative corrections in decays. Comput. Phys. Commun. **66**, 115–128 (1991). https://doi.org/10.1016/0010-4655(91)90012-A

40. LHCb Collaboration, R. Aaij et al., Forward production of Υ mesons in *pp* collisions at $\sqrt{s}$ = 7 and 8 TeV. JHEP **11**, 103 (2015). https://doi.org/10.1007/JHEP11(2015)103. arXiv:1509.02372 [hep-ex]

41. LHCb Collaboration, R. Aaij et al., Measurement of Υ production in *pp* collisions at $\sqrt{s}$ = 13 TeV. JHEP **07**, 134 (2018) [Erratum: JHEP 05, 076 (2019)]. https://doi.org/10.1007/JHEP07(2018)134. arXiv:1804.09214 [hep-ex]

42. C. Bierlich et al., A comprehensive guide to the physics and usage of PYTHIA 8.3. arXiv:2203.11601 [hep-ph]

43. ALICE Collaboration, S. Acharya et al., Studies of J/ψ production at forward rapidity in Pb-Pb collisions at $\sqrt{s_{NN}}$ = 5.02 TeV. JHEP **02**, 041 (2020). https://doi.org/10.1007/JHEP02(2020)041. arXiv:1909.03158 [nucl-ex]

44. M. Butenschön, B.A. Kniehl, Reconciling J/ψ production at HERA, RHIC, Tevatron, and LHC with NRQCD factorization at next-to-leading order. Phys. Rev. Lett. **106**, 022003 (2011). https://doi.org/10.1103/PhysRevLett.106.022003. arXiv:1009.5662 [hep-ph]

45. Y.-Q. Ma, K. Wang, K.-T. Chao, J/ψ (ψ′) production at the Tevatron and LHC at $\mathcal{O}(\alpha_s^4 v^4)$ in nonrelativistic QCD. Phys. Rev. Lett. **106**, 042002 (2011). https://doi.org/10.1103/PhysRevLett.106.042002. arXiv:1009.3655 [hep-ph]

46. Y.-Q. Ma, R. Venugopalan, Comprehensive description of J/ψ Production in proton–proton collisions at collider energies. Phys. Rev. Lett. **113**(19), 192301 (2014). https://doi.org/10.1103/PhysRevLett.113.192301. arXiv:1408.4075 [hep-ph]

47. V. Cheung, R. Vogt, Production and polarization of prompt J/ψ in the improved color evaporation model using the k_T-factorization approach. Phys. Rev. D **98**(11), 114029 (2018). https://doi.org/10.1103/PhysRevD.98.114029. arXiv:1808.02909 [hep-ph]

48. J.-P. Lansberg, H.-S. Shao, N. Yamanaka, Y.-J. Zhang, C. Noûs, Complete NLO QCD study of single- and double-quarkonium hadroproduction in the colour-evaporation model at the Tevatron and the LHC. Phys. Lett. B **807**, 135559 (2020). https://doi.org/10.1016/j.physletb.2020.135559. arXiv:2004.14345 [hep-ph]

49. M. Cacciari, S. Frixione, N. Houdeau, M.L. Mangano, P. Nason, G. Ridolfi, Theoretical predictions for charm and bottom production at the LHC. JHEP **10**, 137 (2012). https://doi.org/10.1007/JHEP10(2012)137. arXiv:1205.6344 [hep-ph]

50. CMS Collaboration, A.M. Sirunyan et al., Measurement of nuclear modification factors of Υ(1S), Υ(2S), and Υ(3S) mesons in PbPb collisions at $\sqrt{s_{NN}}$ = 5.02 TeV. Phys. Lett. B **790**, 270–293 (2019). https://doi.org/10.1016/j.physletb.2019.01.006. arXiv:1805.09215 [hep-ex]

51. V. Cheung, R. Vogt, Production and polarization of prompt Υ(*n*S) in the improved color evaporation model using the k_T-factorization approach. Phys. Rev. D **99**(3), 034007 (2019). https://doi.org/10.1103/PhysRevD.99.034007. arXiv:1811.11570 [hep-ph]

ALICE Collaboration

S. Acharya[142], D. Adamová[97], A. Adler[75], J. Adolfsson[82], G. Aglieri Rinella[34], M. Agnello[30], N. Agrawal[54], Z. Ahammed[142], S. Ahmad[16], S. U. Ahn[77], I. Ahuja[38], Z. Akbar[51], A. Akindinov[94], M. Al-Turany[109], S. N. Alam[16], D. Aleksandrov[90], B. Alessandro[60], H. M. Alfanda[7], R. Alfaro Molina[72], B. Ali[16], Y. Ali[14], A. Alici[25], N. Alizadehvandchali[126], A. Alkin[34], J. Alme[21], T. Alt[69], I. Altsybeev[114], M. N. Anaam[7], C. Andrei[48], D. Andreou[92], A. Andronic[145], M. Angeletti[34], V. Anguelov[106], F. Antinori[57], C. Anuj[16], N. Apadula[81], L. Aphecetche[116], H. Appelshäuser[69], S. Arcelli[25], R. Arnaldi[60], I. C. Arsene[20], M. Arslandok[147], A. Augustinus[34], R. Averbeck[109], S. Aziz[79], M. D. Azmi[16], A. Badalà[56], Y. W. Baek[41], X. Bai[109,130], R. Bailhache[69], Y. Bailung[50], R. Bala[103], A. Balbino[30], A. Baldisseri[139], B. Balis[2], D. Banerjee[4], R. Barbera[26], L. Barioglio[107], M. Barlou[86], G. G. Barnaföldi[146], L. S. Barnby[96], V. Barret[136], C. Bartels[129], K. Barth[34], E. Bartsch[69], F. Baruffaldi[27], N. Bastid[136], S. Basu[82], G. Batigne[116], B. Batyunya[76], D. Bauri[49], J. L. Bazo Alba[113], I. G. Bearden[91], C. Beattie[147], P. Becht[109], I. Belikov[138], A. D. C. Bell Hechavarria[145], F. Bellini[25], R. Bellwied[126], S. Belokurova[114], V. Belyaev[95], G. Bencedi[70,146], S. Beole[24], A. Bercuci[48], Y. Berdnikov[100], A. Berdnikova[106], L. Bergmann[106], M. G. Besoiu[68], L. Betev[34], P. P. Bhaduri[142], A. Bhasin[103], I. R. Bhat[103], M. A. Bhat[4], B. Bhattacharjee[42], P. Bhattacharya[22], L. Bianchi[24], N. Bianchi[52], J. Bielčík[37], J. Bielčíková[97], J. Biernat[119], A. Bilandzic[107], G. Biro[146], S. Biswas[4], J. T. Blair[120], D. Blau[83,90], M. B. Blidaru[109], C. Blume[69], G. Boca[28,58], F. Bock[98], A. Bogdanov[95], S. Boi[22], J. Bok[62], L. Boldizsár[146], A. Bolozdynya[95], M. Bombara[38], P. M. Bond[34], G. Bonomi[58,141], H. Borel[139], A. Borissov[83], H. Bossi[147], E. Botta[24], L. Bratrud[69], P. Braun-Munzinger[109], M. Bregant[122], M. Broz[37], G. E. Bruno[33,108], M. D. Buckland[23,129], D. Budnikov[110], H. Buesching[69], S. Bufalino[30], O. Bugnon[116], P. Buhler[115], Z. Buthelezi[73,133], J. B. Butt[14], A. Bylinkin[128], S. A. Bysiak[119], M. Cai[7,27], H. Caines[147], A. Caliva[109], E. Calvo Villar[113], J. M. M. Camacho[121], R. S. Camacho[45], P. Camerini[23], F. D. M. Canedo[122], F. Carnesecchi[25,34], R. Caron[139], J. Castillo Castellanos[139], E. A. R. Casula[22], F. Catalano[30], C. Ceballos Sanchez[76], P. Chakraborty[49], S. Chandra[142], S. Chapeland[34], M. Chartier[129], S. Chattopadhyay[142], S. Chattopadhyay[111], A. Chauvin[22], T. G. Chavez[45], T. Cheng[7], C. Cheshkov[137], B. Cheynis[137], V. Chibante Barroso[34], D. D. Chinellato[123], S. Cho[62], P. Chochula[34], P. Christakoglou[92], C. H. Christensen[91], P. Christiansen[82], T. Chujo[135], C. Cicalo[55], L. Cifarelli[25], F. Cindolo[54], M. R. Ciupek[109], G. Clai[54,a], J. Cleymans[125,*], F. Colamaria[53], J. S. Colburn[112], D. Colella[33,53,108], A. Collu[81], M. Colocci[34], M. Concas[60,b], G. Conesa Balbastre[80], Z. Conesa del Valle[79], G. Contin[23], J. G. Contreras[37], M. L. Coquet[139], T. M. Cormier[98],

P. Cortese[31], M. R. Cosentino[124], F. Costa[34], S. Costanza[28,58], P. Crochet[136], R. Cruz-Torres[81], E. Cuautle[70], P. Cui[7], L. Cunqueiro[98], A. Dainese[57], F. P. A. Damas[139], M. C. Danisch[106], A. Danu[68], I. Das[111], P. Das[88], P. Das[4], S. Das[4], S. Dash[49], A. De Caro[29], G. de Cataldo[53], L. De Cilladi[24], J. de Cuveland[39], A. De Falco[22], D. De Gruttola[29], N. De Marco[60], C. De Martin[23], S. De Pasquale[29], S. Deb[50], H. F. Degenhardt[122], K. R. Deja[143], L. Dello Stritto[29], W. Deng[7], P. Dhankher[19], D. Di Bari[33], A. Di Mauro[34], R. A. Diaz[8], T. Dietel[125], Y. Ding[7,137], R. Divià[34], D. U. Dixit[19], Ø. Djuvsland[21], U. Dmitrieva[64], J. Do[62], A. Dobrin[68], B. Dönigus[69], A. K. Dubey[142], A. Dubla[92,109], S. Dudi[102], M. Dukhishyam[88], P. Dupieux[136], N. Dzalaiova[13], T. M. Eder[145], R. J. Ehlers[98], V. N. Eikeland[21], F. Eisenhut[69], D. Elia[53], B. Erazmus[116], F. Ercolessi[25], F. Erhardt[101], A. Erokhin[114], M. R. Ersdal[21], B. Espagnon[79], G. Eulisse[34], D. Evans[112], S. Evdokimov[93], L. Fabbietti[107], M. Faggin[27], J. Faivre[80], F. Fan[7], A. Fantoni[52], M. Fasel[98], P. Fecchio[30], A. Feliciello[60], G. Feofilov[114], A. Fernández Téllez[45], A. Ferrero[139], A. Ferretti[24], V. J. G. Feuillard[106], J. Figiel[119], S. Filchagin[110], D. Finogeev[64], F. M. Fionda[21,55], G. Fiorenza[34,108], F. Flor[126], A. N. Flores[120], S. Foertsch[73], S. Fokin[90], E. Fragiacomo[61], E. Frajna[146], U. Fuchs[34], N. Funicello[29], C. Furget[80], A. Furs[64], J. J. Gaardhøje[91], M. Gagliardi[24], A. M. Gago[113], A. Gal[138], C. D. Galvan[121], P. Ganoti[86], C. Garabatos[109], J. R. A. Garcia[45], E. Garcia-Solis[10], K. Garg[116], C. Gargiulo[34], A. Garibli[89], K. Garner[145], P. Gasik[109], E. F. Gauger[120], A. Gautam[128], M. B. Gay Ducati[71], M. Germain[116], J. Ghosh[111], P. Ghosh[142], S. K. Ghosh[4], M. Giacalone[25], P. Gianotti[52], P. Giubellino[60,109], P. Giubilato[27], A. M. C. Glaenzer[139], P. Glässel[106], D. J. Q. Goh[84], V. Gonzalez[144], L. H. González-Trueba[72], S. Gorbunov[39], M. Gorgon[2], L. Görlich[119], S. Gotovac[35], V. Grabski[72], L. K. Graczykowski[143], L. Greiner[81], A. Grelli[63], C. Grigoras[34], V. Grigoriev[95], S. Grigoryan[1,76], F. Grosa[34,60], J. F. Grosse-Oetringhaus[34], R. Grosso[109], G. G. Guardiano[123], R. Guernane[80], M. Guilbaud[116], K. Gulbrandsen[91], T. Gunji[134], W. Guo[7], A. Gupta[103], R. Gupta[103], S. P. Guzman[45], L. Gyulai[146], M. K. Habib[109], C. Hadjidakis[79], H. Hamagaki[84], M. Hamid[7], R. Hannigan[120], M. R. Haque[143], A. Harlenderova[109], J. W. Harris[147], A. Harton[10], J. A. Hasenbichler[34], H. Hassan[98], D. Hatzifotiadou[54], P. Hauer[43], L. B. Havener[147], S. T. Heckel[107], E. Hellbär[109], H. Helstrup[36], T. Herman[37], E. G. Hernandez[45], G. Herrera Corral[9], F. Herrmann[145], K. F. Hetland[36], H. Hillemanns[34], C. Hills[129], B. Hippolyte[138], B. Hofman[63], B. Hohlweger[92], J. Honermann[145], G. H. Hong[148], D. Horak[37], S. Hornung[109], A. Horzyk[2], R. Hosokawa[15], Y. Hou[7], P. Hristov[34], C. Huang[79], C. Hughes[132], P. Huhn[69], L. M. Huhta[127], C. V. Hulse[79], T. J. Humanic[99], H. Hushnud[111], L. A. Husova[145], A. Hutson[126], J. P. Iddon[34,129], R. Ilkaev[110], H. Ilyas[14], M. Inaba[135], G. M. Innocenti[34], M. Ippolitov[90], A. Isakov[97], T. Isidori[128], M. S. Islam[111], M. Ivanov[109], V. Ivanov[100], V. Izucheev[93], M. Jablonski[2], B. Jacak[81], N. Jacazio[34], P. M. Jacobs[81], S. Jadlovska[118], J. Jadlovsky[118], S. Jaelani[63], C. Jahnke[122,123], M. J. Jakubowska[143], A. Jalotra[103], M. A. Janik[143], T. Janson[75], M. Jercic[101], O. Jevons[112], A. A. P. Jimenez[70], F. Jonas[98,145], P. G. Jones[112], J. M. Jowett[34,109], J. Jung[69], M. Jung[69], A. Junique[34], A. Jusko[112], J. Kaewjai[117], P. Kalinak[65], A. S. Kalteyer[109], A. Kalweit[34], V. Kaplin[95], A. Karasu Uysal[78], D. Karatovic[101], O. Karavichev[64], T. Karavicheva[64], P. Karczmarczyk[143], E. Karpechev[64], V. Kashyap[88], A. Kazantsev[90], U. Kebschull[75], R. Keidel[47], D. L. D. Keijdener[63], M. Keil[34], B. Ketzer[43], Z. Khabanova[92], A. M. Khan[7], S. Khan[16], A. Khanzadeev[100], Y. Kharlov[83,93], A. Khatun[16], A. Khuntia[119], B. Kileng[36], B. Kim[17,62], C. Kim[17], D. J. Kim[127], E. J. Kim[74], J. Kim[148], J. S. Kim[41], J. Kim[106], J. Kim[74], M. Kim[106], S. Kim[18], T. Kim[148], S. Kirsch[69], I. Kisel[39], S. Kiselev[94], A. Kisiel[143], J. P. Kitowski[2], J. L. Klay[6], J. Klein[34], S. Klein[81], C. Klein-Bösing[145], M. Kleiner[69], T. Klemenz[107], A. Kluge[34], A. G. Knospe[126], C. Kobdaj[117], M. K. Köhler[106], T. Kollegger[109], A. Kondratyev[76], N. Kondratyeva[95], E. Kondratyuk[93], J. Konig[69], S. A. Konigstorfer[107], P. J. Konopka[34], G. Kornakov[143], S. D. Koryciak[2], A. Kotliarov[97], O. Kovalenko[87], V. Kovalenko[114], M. Kowalski[119], I. Králik[65], A. Kravčáková[38], L. Kreis[109], M. Krivda[65,112], F. Krizek[97], K. Krizkova Gajdosova[37], M. Kroesen[106], M. Krüger[69], E. Kryshen[100], M. Krzewicki[39], V. Kučera[34], C. Kuhn[138], P. G. Kuijer[92], T. Kumaoka[135], D. Kumar[142], L. Kumar[102], N. Kumar[102], S. Kundu[34], P. Kurashvili[87], A. Kurepin[64], A. B. Kurepin[64], A. Kuryakin[110], S. Kushpil[97], J. Kvapil[112], M. J. Kweon[62], J. Y. Kwon[62], Y. Kwon[148], S. L. La Pointe[39], P. La Rocca[26], Y. S. Lai[81], A. Lakrathok[117], M. Lamanna[34], R. Langoy[131], K. Lapidus[34], P. Larionov[34,52], E. Laudi[34], L. Lautner[34,107], R. Lavicka[37,115], T. Lazareva[114], R. Lea[23,58,141], J. Lehrbach[39], R. C. Lemmon[96], I. León Monzón[121], E. D. Lesser[19], M. Lettrich[34,107], P. Lévai[146], X. Li[11], X. L. Li[7], J. Lien[131], R. Lietava[112], B. Lim[17], S. H. Lim[17], V. Lindenstruth[39], A. Lindner[48], C. Lippmann[109], A. Liu[19], D. H. Liu[7], J. Liu[129], I. M. Lofnes[21], V. Loginov[95], C. Loizides[98], P. Loncar[35], J. A. Lopez[106], X. Lopez[136], E. López Torres[8], J. R. Luhder[145], M. Lunardon[27], G. Luparello[61], Y. G. Ma[40], A. Maevskaya[64], M. Mager[34], T. Mahmoud[43], A. Maire[138], M. Malaev[100], N. M. Malik[103], Q. W. Malik[20], S. K. Malik[103], L. Malinina[76,c], D. Mal'Kevich[94], N. Mallick[50], G. Mandaglio[32,56], V. Manko[90], F. Manso[136], V. Manzari[53], Y. Mao[7], G. V. Margagliotti[23], A. Margotti[54], A. Marín[109], C. Markert[120], M. Marquard[69], N. A. Martin[106], P. Martinengo[34], J. L. Martinez[126], M. I. Martínez[45], G. Martínez García[116], S. Masciocchi[109], M. Masera[24], A. Masoni[55], L. Massacrier[79], A. Mastroserio[53,140], A. M. Mathis[107], O. Matonoha[82], P. F. T. Matuoka[122], A. Matyja[119], C. Mayer[119], A. L. Mazuecos[34], F. Mazzaschi[24], M. Mazzilli[34], M. A. Mazzoni[59,*], J. E. Mdhluli[133], A. F. Mechler[69], Y. Melikyan[64], A. Menchaca-Rocha[72], E. Meninno[29,115], A. S. Menon[126], M. Meres[13], S. Mhlanga[73,125], Y. Miake[135], L. Micheletti[60], L. C. Migliorin[137],

D. L. Mihaylov[107], K. Mikhaylov[76,94], A. N. Mishra[146], D. Miśkowiec[109], A. Modak[4], A. P. Mohanty[63], B. Mohanty[88], M. Mohisin Khan[16,d], M. A. Molander[44], Z. Moravcova[91], C. Mordasini[107], D. A. Moreira De Godoy[145], I. Morozov[64], A. Morsch[34], T. Mrnjavac[34], V. Muccifora[52], E. Mudnic[35], D. Mühlheim[145], S. Muhuri[142], J. D. Mulligan[81], A. Mulliri[22], M. G. Munhoz[122], R. H. Munzer[69], H. Murakami[134], S. Murray[125], L. Musa[34], J. Musinsky[65], J. W. Myrcha[143], B. Naik[49,133], R. Nair[87], B. K. Nandi[49], R. Nania[54], E. Nappi[53], A. F. Nassirpour[82], A. Nath[106], C. Nattrass[132], A. Neagu[20], L. Nellen[70], S. V. Nesbo[36], G. Neskovic[39], D. Nesterov[114], B. S. Nielsen[91], S. Nikolaev[90], S. Nikulin[90], V. Nikulin[100], F. Noferini[54], S. Noh[12], P. Nomokonov[76], J. Norman[129], N. Novitzky[135], P. Nowakowski[143], A. Nyanin[90], J. Nystrand[21], M. Ogino[84], A. Ohlson[82], V. A. Okorokov[95], J. Oleniacz[143], A. C. Oliveira Da Silva[132], M. H. Oliver[147], A. Onnerstad[127], C. Oppedisano[60], A. Ortiz Velasquez[70], T. Osako[46], A. Oskarsson[82], J. Otwinowski[119], M. Oya[46], K. Oyama[84], Y. Pachmayer[106], S. Padhan[49], D. Pagano[58,141], G. Paić[70], A. Palasciano[53], J. Pan[144], S. Panebianco[139], J. Park[62], J. E. Parkkila[127], S. P. Pathak[126], R. N. Patra[34,103], B. Paul[22], H. Pei[7], T. Peitzmann[63], X. Peng[7], L. G. Pereira[71], H. Pereira Da Costa[139], D. Peresunko[83,90], G. M. Perez[8], S. Perrin[139], Y. Pestov[5], V. Petráček[37], M. Petrovici[48], R. P. Pezzi[71,116], S. Piano[61], M. Pikna[13], P. Pillot[116], O. Pinazza[34,54], L. Pinsky[126], C. Pinto[26], S. Pisano[52], M. Płoskoń[81], M. Planinic[101], F. Pliquett[69], M. G. Poghosyan[98], B. Polichtchouk[93], S. Politano[30], N. Poljak[101], A. Pop[48], S. Porteboeuf-Houssais[136], J. Porter[81], V. Pozdniakov[76], S. K. Prasad[4], R. Preghenella[54], F. Prino[60], C. A. Pruneau[144], I. Pshenichnov[64], M. Puccio[34], S. Qiu[92], L. Quaglia[24], R. E. Quishpe[126], S. Ragoni[112], A. Rakotozafindrabe[139], L. Ramello[31], F. Rami[138], S. A. R. Ramirez[45], A. G. T. Ramos[33], T. A. Rancien[80], R. Raniwala[104], S. Raniwala[104], S. S. Räsänen[44], R. Rath[50], I. Ravasenga[92], K. F. Read[98,132], A. R. Redelbach[39], K. Redlich[87,e], A. Rehman[21], P. Reichelt[69], F. Reidt[34], H. A. Reme-ness[36], Z. Rescakova[38], K. Reygers[106], A. Riabov[100], V. Riabov[100], T. Richert[82], M. Richter[20], W. Riegler[34], F. Riggi[26], C. Ristea[68], M. Rodríguez Cahuantzi[45], K. Røed[20], R. Rogalev[93], E. Rogochaya[76], T. S. Rogoschinski[69], D. Rohr[34], D. Röhrich[21], P. F. Rojas[45], P. S. Rokita[143], F. Ronchetti[52], A. Rosano[32,56], E. D. Rosas[70], A. Rossi[57], A. Roy[50], P. Roy[111], S. Roy[49], N. Rubini[25], O. V. Rueda[82], D. Ruggiano[143], R. Rui[23], B. Rumyantsev[76], P. G. Russek[2], R. Russo[92], A. Rustamov[89], E. Ryabinkin[90], Y. Ryabov[100], A. Rybicki[119], H. Rytkonen[127], W. Rzesa[143], O. A. M. Saarimaki[44], R. Sadek[116], S. Sadovsky[93], J. Saetre[21], K. Šafařík[37], S. K. Saha[142], S. Saha[88], B. Sahoo[49], P. Sahoo[49], R. Sahoo[50], S. Sahoo[66], D. Sahu[50], P. K. Sahu[66], J. Saini[142], S. Sakai[135], M. P. Salvan[109], S. Sambyal[103], V. Samsonov[95,100,*], D. Sarkar[144], N. Sarkar[142], P. Sarma[42], V. M. Sarti[107], M. H. P. Sas[147], J. Schambach[98], H. S. Scheid[69], C. Schiaua[48], R. Schicker[106], A. Schmah[106], C. Schmidt[109], H. R. Schmidt[105], M. O. Schmidt[34,106], M. Schmidt[105], N. V. Schmidt[69,98], A. R. Schmier[132], R. Schotter[138], J. Schukraft[34], K. Schwarz[109], K. Schweda[109], G. Scioli[25], E. Scomparin[60], J. E. Seger[15], Y. Sekiguchi[134], D. Sekihata[134], I. Selyuzhenkov[95,109], S. Senyukov[138], J. J. Seo[62], D. Serebryakov[64], L. Šerkšnytė[107], A. Sevcenco[68], T. J. Shaba[73], A. Shabanov[64], A. Shabetai[116], R. Shahoyan[34], W. Shaikh[111], A. Shangaraev[93], A. Sharma[102], H. Sharma[119], M. Sharma[103], N. Sharma[102], S. Sharma[103], U. Sharma[103], O. Sheibani[126], K. Shigaki[46], M. Shimomura[85], M. Shirinkin[94], Q. Shou[40], Y. Sibiriak[90], S. Siddhanta[55], T. Siemiarczuk[87], T. F. Silva[122], D. Silvermyr[82], T. Simantathammakul[117], G. Simonetti[34], B. Singh[107], R. Singh[88], R. Singh[103], R. Singh[50], V. K. Singh[142], V. Singhal[142], T. Sinha[111], B. Sitar[13], M. Sitta[31], T. B. Skaali[20], G. Skorodumovs[106], M. Slupecki[44], N. Smirnov[147], R. J. M. Snellings[63], C. Soncco[113], J. Song[126], A. Songmoolnak[117], F. Soramel[27], S. Sorensen[132], I. Sputowska[119], J. Stachel[106], I. Stan[68], P. J. Steffanic[132], S. F. Stiefelmaier[106], D. Stocco[116], I. Storehaug[20], M. M. Storetvedt[36], P. Stratmann[145], C. P. Stylianidis[92], A. A. P. Suaide[122], C. Suire[79], M. Sukhanov[64], M. Suljic[34], R. Sultanov[94], V. Sumberia[103], S. Sumowidagdo[51], S. Swain[66], A. Szabo[13], I. Szarka[13], U. Tabassam[14], S. F. Taghavi[107], G. Taillepied[136], J. Takahashi[123], G. J. Tambave[21], S. Tang[7,136], Z. Tang[130], J. D. Tapia Takaki[128,f], M. Tarhini[116], M. G. Tarzila[48], A. Tauro[34], G. Tejeda Muñoz[45], A. Telesca[34], L. Terlizzi[24], C. Terrevoli[126], G. Tersimonov[3], S. Thakur[142], D. Thomas[120], R. Tieulent[137], A. Tikhonov[64], A. R. Timmins[126], M. Tkacik[118], A. Toia[69], N. Topilskaya[64], M. Toppi[52], F. Torales-Acosta[19], T. Tork[79], S. R. Torres[37], A. Trifiró[32,56], S. Tripathy[54,70], T. Tripathy[49], S. Trogolo[27,34], V. Trubnikov[3], W. H. Trzaska[127], T. P. Trzcinski[143], A. Tumkin[110], R. Turrisi[57], T. S. Tveter[20], K. Ullaland[21], A. Uras[137], M. Urioni[58,141], G. L. Usai[22], M. Vala[38], N. Valle[28,58], S. Vallero[60], L. V. R. van Doremalen[63], M. van Leeuwen[92], P. Vande Vyvre[34], D. Varga[146], Z. Varga[146], M. Varga-Kofarago[146], M. Vasileiou[86], A. Vasiliev[90], O. Vázquez Doce[52,107], V. Vechernin[114], E. Vercellin[24], S. Vergara Limón[45], L. Vermunt[63], R. Vértesi[146], M. Verweij[63], L. Vickovic[35], Z. Vilakazi[133], O. Villalobos Baillie[112], G. Vino[53], A. Vinogradov[90], T. Virgili[29], V. Vislavicius[91], A. Vodopyanov[76], B. Volkel[34,106], M. A. Völkl[106], K. Voloshin[94], S. A. Voloshin[144], G. Volpe[33], B. von Haller[34], I. Vorobyev[107], D. Voscek[118], N. Vozniuk[64], J. Vrláková[38], B. Wagner[21], C. Wang[40], D. Wang[40], M. Weber[115], R. J. G. V. Weelden[92], A. Wegrzynek[34], S. C. Wenzel[34], J. P. Wessels[145], J. Wiechula[69], J. Wikne[20], G. Wilk[87], J. Wilkinson[109], G. A. Willems[145], B. Windelband[106], M. Winn[139], W. E. Witt[132], J. R. Wright[120], W. Wu[40], Y. Wu[130], R. Xu[7], A. K. Yadav[142], S. Yalcin[78], Y. Yamaguchi[46], K. Yamakawa[46], S. Yang[21], S. Yano[46], Z. Yin[7], I. -K. Yoo[17], J. H. Yoon[62], S. Yuan[21], A. Yuncu[106], V. Zaccolo[23], C. Zampolli[34], H. J. C. Zanoli[63], N. Zardoshti[34], A. Zarochentsev[114], P. Závada[67], N. Zaviyalov[110], M. Zhalov[100], B. Zhang[7], S. Zhang[40],

X. Zhang[7], Y. Zhang[130], V. Zherebchevskii[114], Y. Zhi[11], N. Zhigareva[94], D. Zhou[7], Y. Zhou[91], J. Zhu[7,109], Y. Zhu[7], G. Zinovjev[3], N. Zurlo[58,141]

1 A.I. Alikhanyan National Science Laboratory (Yerevan Physics Institute) Foundation, Yerevan, Armenia

2 AGH University of Science and Technology, Kraków, Poland

3 Bogolyubov Institute for Theoretical Physics, National Academy of Sciences of Ukraine, Kiev, Ukraine

4 Department of Physics and Centre for Astroparticle Physics and Space Science (CAPSS), Bose Institute, Kolkata, India

5 Budker Institute for Nuclear Physics, Novosibirsk, Russia

6 California Polytechnic State University, San Luis Obispo, CA, USA

7 Central China Normal University, Wuhan, China

8 Centro de Aplicaciones Tecnológicas y Desarrollo Nuclear (CEADEN), Havana, Cuba

9 Centro de Investigación y de Estudios Avanzados (CINVESTAV), Mexico City and Mérida, Mexico

10 Chicago State University, Chicago, IL, USA

11 China Institute of Atomic Energy, Beijing, China

12 Chungbuk National University, Cheongju, Republic of Korea

13 Faculty of Mathematics, Physics and Informatics, Comenius University Bratislava, Bratislava, Slovakia

14 COMSATS University Islamabad, Islamabad, Pakistan

15 Creighton University, Omaha, NE, USA

16 Department of Physics, Aligarh Muslim University, Aligarh, India

17 Department of Physics, Pusan National University, Pusan, Republic of Korea

18 Department of Physics, Sejong University, Seoul, Republic of Korea

19 Department of Physics, University of California, Berkeley, CA, USA

20 Department of Physics, University of Oslo, Oslo, Norway

21 Department of Physics and Technology, University of Bergen, Bergen, Norway

22 Dipartimento di Fisica dell'Università and Sezione INFN, Cagliari, Italy

23 Dipartimento di Fisica dell'Università and Sezione INFN, Trieste, Italy

24 Dipartimento di Fisica dell'Università and Sezione INFN, Turin, Italy

25 Dipartimento di Fisica e Astronomia dell'Università and Sezione INFN, Bologna, Italy

26 Dipartimento di Fisica e Astronomia dell'Università and Sezione INFN, Catania, Italy

27 Dipartimento di Fisica e Astronomia dell'Università and Sezione INFN, Padua, Italy

28 Dipartimento di Fisica e Nucleare e Teorica, Università di Pavia, Pavia, Italy

29 Dipartimento di Fisica 'E.R. Caianiello' dell'Università and Gruppo Collegato INFN, Salerno, Italy

30 Dipartimento DISAT del Politecnico and Sezione INFN, Turin, Italy

31 Dipartimento di Scienze e Innovazione Tecnologica dell'Università del Piemonte Orientale and INFN Sezione di Torino, Alessandria, Italy

32 Dipartimento di Scienze MIFT, Università di Messina, Messina, Italy

33 Dipartimento Interateneo di Fisica 'M. Merlin' and Sezione INFN, Bari, Italy

34 European Organization for Nuclear Research (CERN), Geneva, Switzerland

35 Faculty of Electrical Engineering, Mechanical Engineering and Naval Architecture, University of Split, Split, Croatia

36 Faculty of Engineering and Science, Western Norway University of Applied Sciences, Bergen, Norway

37 Faculty of Nuclear Sciences and Physical Engineering, Czech Technical University in Prague, Prague, Czech Republic

38 Faculty of Science, P.J. Šafárik University, Košice, Slovakia

39 Frankfurt Institute for Advanced Studies, Johann Wolfgang Goethe-Universität Frankfurt, Frankfurt, Germany

40 Fudan University, Shanghai, China

41 Gangneung-Wonju National University, Gangneung, Republic of Korea

42 Department of Physics, Gauhati University, Guwahati, India

43 Helmholtz-Institut für Strahlen- und Kernphysik, Rheinische Friedrich-Wilhelms-Universität Bonn, Bonn, Germany

44 Helsinki Institute of Physics (HIP), Helsinki, Finland

45 High Energy Physics Group, Universidad Autónoma de Puebla, Puebla, Mexico

46 Hiroshima University, Hiroshima, Japan

47 Hochschule Worms, Zentrum für Technologietransfer und Telekommunikation (ZTT), Worms, Germany

48 Horia Hulubei National Institute of Physics and Nuclear Engineering, Bucharest, Romania

49 Indian Institute of Technology Bombay (IIT), Mumbai, India

[50] Indian Institute of Technology Indore, Indore, India

[51] Indonesian Institute of Sciences, Jakarta, Indonesia

[52] INFN, Laboratori Nazionali di Frascati, Frascati, Italy

[53] INFN, Sezione di Bari, Bari, Italy

[54] INFN, Sezione di Bologna, Bologna, Italy

[55] INFN, Sezione di Cagliari, Cagliari, Italy

[56] INFN, Sezione di Catania, Catania, Italy

[57] INFN, Sezione di Padova, Padua, Italy

[58] INFN, Sezione di Pavia, Pavia, Italy

[59] INFN, Sezione di Roma, Rome, Italy

[60] INFN, Sezione di Torino, Turin, Italy

[61] INFN, Sezione di Trieste, Trieste, Italy

[62] Inha University, Incheon, Republic of Korea

[63] Institute for Gravitational and Subatomic Physics (GRASP), Utrecht University/Nikhef, Utrecht, The Netherlands

[64] Institute for Nuclear Research, Academy of Sciences, Moscow, Russia

[65] Institute of Experimental Physics, Slovak Academy of Sciences, Košice, Slovakia

[66] Institute of Physics, Homi Bhabha National Institute, Bhubaneswar, India

[67] Institute of Physics of the Czech Academy of Sciences, Prague, Czech Republic

[68] Institute of Space Science (ISS), Bucharest, Romania

[69] Institut für Kernphysik, Johann Wolfgang Goethe-Universität Frankfurt, Frankfurt, Germany

[70] Instituto de Ciencias Nucleares, Universidad Nacional Autónoma de México, Mexico City, Mexico

[71] Instituto de Física, Universidade Federal do Rio Grande do Sul (UFRGS), Porto Alegre, Brazil

[72] Instituto de Física, Universidad Nacional Autónoma de México, Mexico City, Mexico

[73] iThemba LABS, National Research Foundation, Somerset West, South Africa

[74] Jeonbuk National University, Jeonju, Republic of Korea

[75] Johann-Wolfgang-Goethe Universität Frankfurt Institut für Informatik, Fachbereich Informatik und Mathematik, Frankfurt, Germany

[76] Joint Institute for Nuclear Research (JINR), Dubna, Russia

[77] Korea Institute of Science and Technology Information, Daejeon, Republic of Korea

[78] KTO Karatay University, Konya, Turkey

[79] Laboratoire de Physique des 2 Infinis, Irène Joliot-Curie, Orsay, France

[80] Laboratoire de Physique Subatomique et de Cosmologie, Université Grenoble-Alpes, CNRS-IN2P3, Grenoble, France

[81] Lawrence Berkeley National Laboratory, Berkeley, CA, USA

[82] Division of Particle Physics, Department of Physics, Lund University, Lund, Sweden

[83] Moscow Institute for Physics and Technology, Moscow, Russia

[84] Nagasaki Institute of Applied Science, Nagasaki, Japan

[85] Nara Women's University (NWU), Nara, Japan

[86] Department of Physics, School of Science, National and Kapodistrian University of Athens, Athens, Greece

[87] National Centre for Nuclear Research, Warsaw, Poland

[88] National Institute of Science Education and Research, Homi Bhabha National Institute, Jatni, India

[89] National Nuclear Research Center, Baku, Azerbaijan

[90] National Research Centre Kurchatov Institute, Moscow, Russia

[91] Niels Bohr Institute, University of Copenhagen, Copenhagen, Denmark

[92] Nikhef, National institute for subatomic physics, Amsterdam, The Netherlands

[93] NRC Kurchatov Institute IHEP, Protvino, Russia

[94] NRC «Kurchatov»Institute-ITEP, Moscow, Russia

[95] NRNU Moscow Engineering Physics Institute, Moscow, Russia

[96] Nuclear Physics Group, STFC Daresbury Laboratory, Daresbury, UK

[97] Nuclear Physics Institute of the Czech Academy of Sciences, Řež u Prahy, Czech Republic

[98] Oak Ridge National Laboratory, Oak Ridge, TN, USA

[99] Ohio State University, Columbus, OH, USA

[100] Petersburg Nuclear Physics Institute, Gatchina, Russia

[101] Physics Department, Faculty of science, University of Zagreb, Zagreb, Croatia

[102] Physics Department, Panjab University, Chandigarh, India

[103] Physics Department, University of Jammu, Jammu, India

[104] Physics Department, University of Rajasthan, Jaipur, India

[105] Physikalisches Institut, Eberhard-Karls-Universität Tübingen, Tübingen, Germany

[106] Physikalisches Institut, Ruprecht-Karls-Universität Heidelberg, Heidelberg, Germany

[107] Physik Department, Technische Universität München, Munich, Germany

[108] Politecnico di Bari and Sezione INFN, Bari, Italy

[109] Research Division and ExtreMe Matter Institute EMMI, GSI Helmholtzzentrum für Schwerionenforschung GmbH, Darmstadt, Germany

[110] Russian Federal Nuclear Center (VNIIEF), Sarov, Russia

[111] Saha Institute of Nuclear Physics, Homi Bhabha National Institute, Kolkata, India

[112] School of Physics and Astronomy, University of Birmingham, Birmingham, UK

[113] Sección Física, Departamento de Ciencias, Pontificia Universidad Católica del Perú, Lima, Peru

[114] St. Petersburg State University, St. Petersburg, Russia

[115] Stefan Meyer Institut für Subatomare Physik (SMI), Vienna, Austria

[116] SUBATECH, IMT Atlantique, Université de Nantes, CNRS-IN2P3, Nantes, France

[117] Suranaree University of Technology, Nakhon Ratchasima, Thailand

[118] Technical University of Košice, Košice, Slovakia

[119] The Henryk Niewodniczanski Institute of Nuclear Physics, Polish Academy of Sciences, Kraków, Poland

[120] The University of Texas at Austin, Austin, TX, USA

[121] Universidad Autónoma de Sinaloa, Culiacán, Mexico

[122] Universidade de São Paulo (USP), São Paulo, Brazil

[123] Universidade Estadual de Campinas (UNICAMP), Campinas, Brazil

[124] Universidade Federal do ABC, Santo Andre, Brazil

[125] University of Cape Town, Cape Town, South Africa

[126] University of Houston, Houston, TX, USA

[127] University of Jyväskylä, Jyväskylä, Finland

[128] University of Kansas, Lawrence, KS, USA

[129] University of Liverpool, Liverpool, UK

[130] University of Science and Technology of China, Hefei, China

[131] University of South-Eastern Norway, Tonsberg, Norway

[132] University of Tennessee, Knoxville, TN, USA

[133] University of the Witwatersrand, Johannesburg, South Africa

[134] University of Tokyo, Tokyo, Japan

[135] University of Tsukuba, Tsukuba, Japan

[136] Université Clermont Auvergne, CNRS/IN2P3, LPC, Clermont-Ferrand, France

[137] Université de Lyon, CNRS/IN2P3, Institut de Physique des 2 Infinis de Lyon, Lyon, France

[138] Université de Strasbourg, CNRS, IPHC UMR 7178, 67000 Strasbourg, France

[139] Départment de Physique Nucléaire (DPhN), IRFU, Université Paris-Saclay Centre d'Etudes de Saclay (CEA), Saclay, France

[140] Università degli Studi di Foggia, Foggia, Italy

[141] Università di Brescia, Brescia, Italy

[142] Variable Energy Cyclotron Centre, Homi Bhabha National Institute, Kolkata, India

[143] Warsaw University of Technology, Warsaw, Poland

[144] Wayne State University, Detroit, MI, USA

[145] Institut für Kernphysik, Westfälische Wilhelms-Universität Münster, Münster, Germany

[146] Wigner Research Centre for Physics, Budapest, Hungary

[147] Yale University, New Haven, CT, USA

[148] Yonsei University, Seoul, Republic of Korea

[a] Also at Italian National Agency for New Technologies, Energy and Sustainable Economic Development (ENEA), Bologna, Italy

[b] Also at Dipartimento DET del Politecnico di Torino, Turin, Italy

[c] Also at M.V. Lomonosov Moscow State University, D.V. Skobeltsyn Institute of Nuclear Physics, Moscow, Russia

[d] Also at Department of Applied Physics, Aligarh Muslim University, Aligarh, India

[e] Also at Institute of Theoretical Physics, University of Wroclaw, Wroclaw, Poland

[f] Also at University of Kansas, Lawrence, KS, USA

  * Deceased